Article

Glycosphingolipid synthesis mediates immune evasion in *KRAS*-driven cancer

https://doi.org/10.1038/s41586-024-07787-1

Received: 29 January 2023

Accepted: 3 July 2024

Published online: 07 August 2024

Check for updates

Mariluz Soula[1], Gokhan Unlu[1], Rachel Welch[1], Aleksey Chudnovskiy[2], Beste Uygur[1], Vyom Shah[3], Hanan Alwaseem[4], Paul Bunk[3], Vishvak Subramanyam[5,6,7,8], Hsi-Wen Yeh[1], Artem Khan[1], Søren Heissel[4], Hani Goodarzi[5,6,7,8], Gabriel D. Victora[2], Semir Beyaz[3] & Kıvanç Birsoy[1]✉

Cancer cells frequently alter their lipids to grow and adapt to their environment[1–3]. Despite the critical functions of lipid metabolism in membrane physiology, signalling and energy production, how specific lipids contribute to tumorigenesis remains incompletely understood. Here, using functional genomics and lipidomic approaches, we identified de novo sphingolipid synthesis as an essential pathway for cancer immune evasion. Synthesis of sphingolipids is surprisingly dispensable for cancer cell proliferation in culture or in immunodeficient mice but required for tumour growth in multiple syngeneic models. Blocking sphingolipid production in cancer cells enhances the anti-proliferative effects of natural killer and $CD8^+$ T cells partly via interferon-γ (IFNγ) signalling. Mechanistically, depletion of glycosphingolipids increases surface levels of IFNγ receptor subunit 1 (IFNGR1), which mediates IFNγ-induced growth arrest and pro-inflammatory signalling. Finally, pharmacological inhibition of glycosphingolipid synthesis synergizes with checkpoint blockade therapy to enhance anti-tumour immune response. Altogether, our work identifies glycosphingolipids as necessary and limiting metabolites for cancer immune evasion.

Lipids constitute a complex and diverse group of biomolecules that are critical for membrane homeostasis, signalling and energy production[4,5]. Rapidly proliferating cancer cells require a constant supply of lipids to support cell growth and adaptation to their environment. Metabolic genes involved in the synthesis and uptake of lipids are downstream effectors of oncogenic alterations and are commonly upregulated in tumours[6]. These changes in lipid metabolism are also influenced by the tumour microenvironment (TME) and organismal metabolism. Indeed, hypoxic tumour cells increase lipid scavenging to compensate for reduced fatty acid desaturation[2,3,7], and saturated lipids in the TME can protect cancer cells from oxidative damage[1]. Furthermore, dietary lipids obtained upon high fat feeding promote tumour initiation[8,9], metastasis[10,11] and immune evasion in mouse models[12–14]. In some instances, the tumorigenic effects of lipids are mediated by consequential alterations in the function of immune cells in the TME[12,15]. Although excess lipids are often associated with tumour progression, precisely which lipid species contribute to tumorigenesis and immune evasion are poorly understood.

Sphingolipid synthesis promotes immune evasion

To identify lipid pathways involved in cancer immune evasion, we performed parallel in vivo genetic screens using HY15549, a *Kras*-mutant mouse pancreatic ductal adenocarcinoma (PDAC) cell line transduced with a library containing single guide RNAs (sgRNAs) targeting 296 genes involved in lipid metabolism pathways including fatty acid synthesis and oxidation, lipid scavenging and cholesterol and phospholipid synthesis and salvage (Fig. 1a). These cells were engrafted into the flanks of C57BL/6J immunocompetent mice, myeloablated controls and NOD-SCID gamma (NSG) mice, which lack mature T, B and natural killer (NK) cells (Fig. 1b). Of note, myeloablated mice were included to account for the metabolic and genetic differences between C57BL/6J and NSG mice (Extended Data Fig. 1a). Gene scores were calculated as the median $\log_2$-transformed fold change in the abundance of all sgRNAs targeting each gene and differential gene essentiality was determined by comparing gene scores between the tumours grown in immunocompetent and immunocompromised mice. KEGG pathway analysis of the top 60 differentially expressed genes in C57BL/6J compared to myeloablated C57BL/6J or NSG mice revealed that synthesis of membrane lipids including sphingolipids, phosphatidylcholine and phosphatidylethanolamine was required for immune evasion (Fig. 1c,d and Extended Data Fig. 1b). An independent lipidomic analysis revealed a significant enrichment for sphingolipids in tumours grown in immunocompetent mice, but not in those grown in immunodeficient mice (Fig. 1e and Extended Data Fig. 1c–i). Given their upregulation in tumours and distinct roles in oncogenic functions, we focused our attention on understanding how sphingolipids mediate tumour immune evasion.

Sphingolipids are structural components of cellular membranes, but bioactive sphingolipids such as ceramide-1-phosphate or

[1]Laboratory of Metabolic Regulation and Genetics, The Rockefeller University, New York, NY, USA. [2]Laboratory of Lymphocyte Dynamics, The Rockefeller University, New York, NY, USA. [3]Cold Spring Harbor Laboratory, Cold Spring Harbor, New York, USA. [4]The Proteomics Resource Center, The Rockefeller University, New York, NY, USA. [5]Department of Biochemistry and Biophysics, University of California, San Francisco, San Francisco, CA, USA. [6]Department of Urology, University of California, San Francisco, San Francisco, CA, USA. [7]Helen Diller Family Comprehensive Cancer Center, University of California, San Francisco, San Francisco, CA, USA. [8]Bakar Computational Health Sciences Institute, University of California, San Francisco, San Francisco, CA, USA. ✉e-mail: kbirsoy@rockefeller.edu

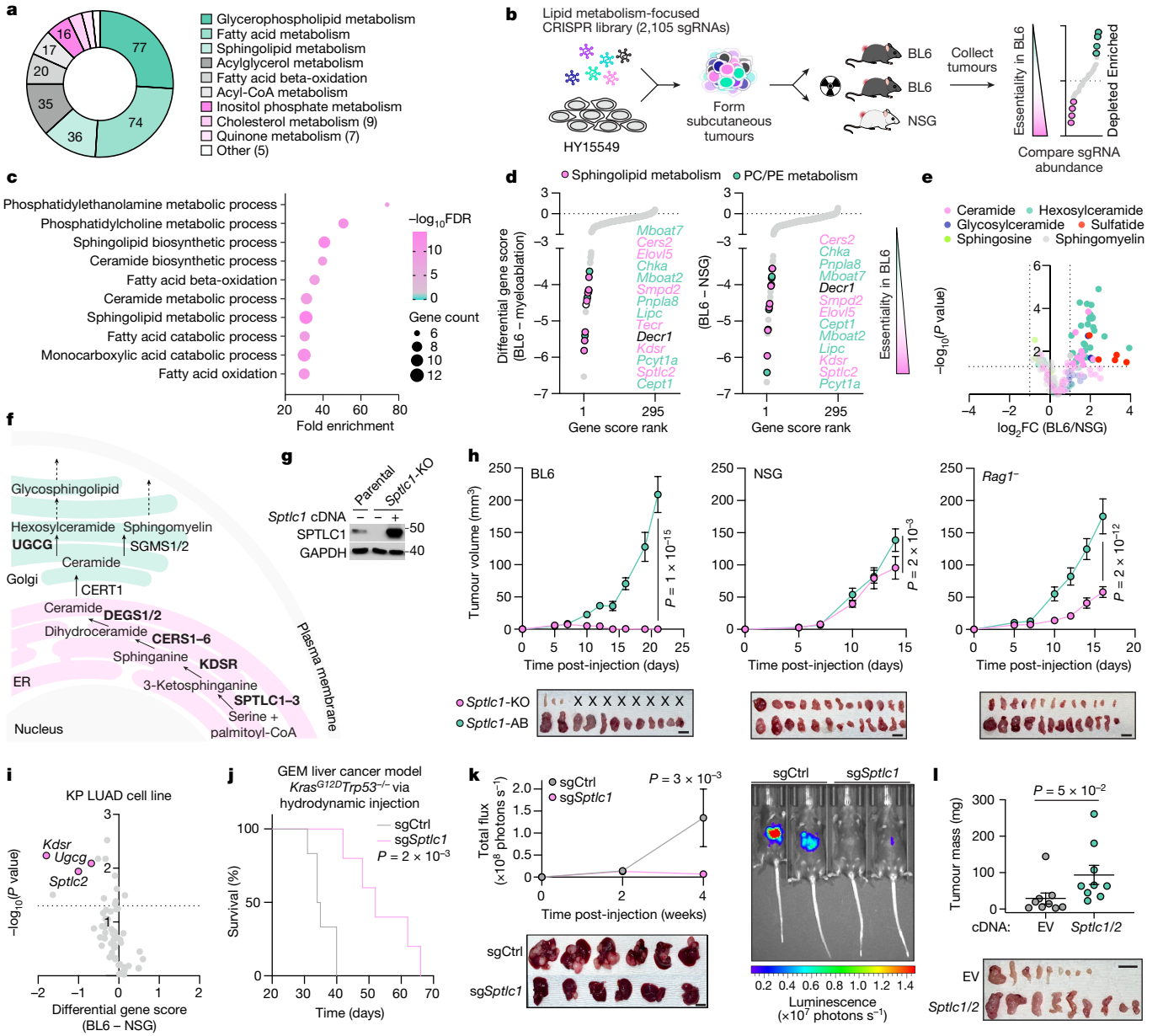

Fig. 1 | The essential role of sphingolipid synthesis in cancer immune evasion. a, Distribution of genes in the focused CRISPR library. **b**, HY15549 cells transduced with the lipid metabolism library were injected subcutaneously into C57BL/6J (BL6), myeloablated BL6 or NSG mice. Tumours were collected and guide RNA (sgRNA) abundance was determined. $n \geq 3$ mice per group. **c**, KEGG pathway analysis of the top 60 essential genes in C57BL/6J mice vers us myeolablated C57BL/6J or NSG mice. KEGG terms are ranked by fold enrichment. The log-transformed false discovery rate is colour-coded; circle size corresponds to the total number of genes in the set. **d**, Ranks of differential gene scores between C57BL/6J and myeloablated or NSG mice. Highlighted genes are among the top 25 scoring genes. PC/PE, phosphatidylcholine and phosphatidylethanolamine. **e**, The $\log_2$-transformed fold change (FC) in ceramide-derived species between HY15549 tumours grown in C57BL/6J or NSG mice. $n = 3$ mice per group. **f**, Scoring genes (bold) in the sphingolipid metabolism pathway. De novo synthesis begins in the endoplasmic reticulum (ER). Ceramides are transferred to the Golgi and modified to sphingomyelin or glycosphingolipids, which make up cellular membranes. Sphingolipids in membranes or the lysosome are catabolized into ceramides and sphingosine via the salvage pathway. **g**, Immunoblot of SPTLC1 in wild-type HY15549 cells or in a *Sptlc1*-KO and *Sptlc1* cDNA-expressing (*Sptlc1*-AB) clonal pair. Full blot is shown in Extended Data Fig. 2a. **h**, Tumour volume of *Sptlc1*-KO (pink) and *Sptlc1*-AB (blue) HY15549 cells grown in C57BL/6J, NSG, or *Rag1*$^-$ mice. Data are mean ± s.e.m.; $n = 6$ (C57BL/6J) or 7 (NSG, *Rag1*$^-$) mice per group. Tumours are shown below. Scale bars, 1 cm. X indicates that tumours were not detected at the endpoint. **i**, Gene essentiality in KP LUAD tumours grown in C57BL/6J versus NSG mice. The dotted line represents $P = 0.05$. De novo sphingolipid synthesis genes are highlighted. $n \geq 4$ mice per group. **j**, Survival of C57BL/6J mice bearing *Kras*^{G12D}*Trp53*$^{-/-}$ liver tumours generated by hydrodynamic gene delivery expressing control sgRNA (sgCtrl; $n = 6$) or *Sptlc1* sgRNA (sg*Sptlc1*; $n = 5$). **k**, Top left, luciferase flux from *Kras*^{G12D}*Trp53*$^{-/-}$ liver tumours expressing sgCtrl ($n = 6$) or sg*Sptlc1* ($n = 5$) generated by hydrodynamic gene delivery in C57BL/6J mice. A representative image (right) and tumours (bottom left). Data are mean ± s.e.m. Scale bar, 1 cm **l**, Tumour mass (top) and images (bottom) of double-empty vector wild-type (EV) or *Sptlc1*/*Sptlc2* double-overexpression (*Sptlc1/2*) HY15549 tumours grown in C57BL/6J mice. Data are mean ± s.e.m.; $n = 5$ mice per group. Scale bar, 1 cm.

sphingosine-1-phosphate also have diverse biological roles in growth regulation, migration, cell death and immune responses[16]. De novo synthesis of sphingolipids begins in the endoplasmic reticulum, with the rate-limiting step being catalysed by serine palmitoyl transferase (SPT), an enzyme made up of two subunits, SPTLC1 and SPTLC2[17]. SPT combines palmitoyl-CoA and serine to produce 3-ketosphinganine,

which after a series of steps is converted to ceramides, precursors of more complex membrane sphingolipids such as sphingomyelin and glycosphingolipids[18]. In addition to being integral parts of cellular membranes, these complex lipids are enriched in membrane lipid nanodomains and caveolae and thereby regulate signal transduction, cell–cell interactions, and membrane structure[19]. Remarkably, genes that encode the enzymes in the de novo ceramide synthesis pathway (*Sptlc1*, *Sptlc2*, *Kdsr*, *Cers* and *Degs*) and the enzyme that generates the precursor to all glycosphingolipids (*Ugcg*) scored as essential for tumour growth in immunocompetent mice (Fig. 1d and Extended Data Fig. 1b). By contrast, none of the genes associated with the production of sphingosine, ceramide-1-phosphate or sphingosine-1-phosphate scored in our analysis, raising the possibility that membrane glycosphingolipid production may be particularly relevant for immune evasion (Fig. 1f).

To begin to understand why cancer cells require de novo sphingolipid synthesis for immune evasion, we first generated *Sptlc1*-knockout (KO) or *Sptlc2*-KO HY15549 cells and their isogenic counterparts expressing sgRNA-resistant *Sptlc1* or *Sptlc2* cDNA and confirmed depletion of ceramide- and sphingolipid-derived lipid species in knockout cells (Fig. 1g and Extended Data Fig. 2a–f). Notably, the sphingolipid depletion observed in vitro upon SPT loss was partially recapitulated in cells grown as tumours in immunocompetent mice. Differences observed in tumour samples compared with cells grown in culture may be due to the presence of other cell types that contribute to sphingolipid abundance in the TME (Extended Data Fig. 2g). Consistent with the screen results, loss of sphingolipid synthesis severely impaired tumour growth in C57BL/6J mice, but not in NSG mice (Fig. 1h and Extended Data Fig. 3a). Short hairpin RNA (shRNA)- and sgRNA-mediated knockdown of *Sptlc1* or *Sptlc2* also blunted tumour growth in immunocompetent mice (Extended Data Fig. 3b,c) and similar results were observed in an orthotopic pancreas cancer model, indicating that the tumoral requirement for sphingolipids is independent of the organ environment (Extended Data Fig. 3d). *Sptlc1* loss partially affected tumour growth in *Rag1*$^{-}$ mice, which have functional NK cells but lack mature T and B cells, suggesting that both adaptive and innate immune systems contribute to tumour surveillance of *Sptlc1*-KO or *Sptlc2*-KO tumours (Fig. 1h and Extended Data Fig. 3a). We next explored whether de novo sphingolipid synthesis is necessary for immune escape in other cancer types. To test this in an unbiased way, we performed small-scale screens using a sphingolipid metabolism-focused CRISPR library that targets 82 genes in a *Kras*-mutant C57BL/6J syngeneic lung (KP LUAD, *Kras*$^{G12D/+}$*Trp53*$^{-/-}$; Extended Data Fig. 4a). In line with the original screen results, de novo sphingolipid synthesis genes were required for immune evasion in KP LUAD tumours (Fig. 1i). Additionally, using a genetically engineered intrahepatic cholangiocarcinoma *Kras*^{G12D}*Trp53*$^{-/-}$ model generated by hydrodynamic gene delivery in C57BL/6J mice, we observed that *Sptlc1* loss significantly prolonged survival and impaired the growth of liver tumours (Fig. 1j,k). To test whether SPT function is limiting for immune evasion, we next simultaneously overexpressed *Sptlc1* and *Sptlc2* in HY15549 cells and compared tumour growth in C57BL/6J and NSG mice (Extended Data Fig. 4b,c). Remarkably, increasing SPT function enhanced tumour growth in immunocompetent mice, but not in immunocompromised mice (Fig. 1l and Extended Data Fig. 4d). Consistent with this, high expression of *SPTLC1*, *SPTLC2* and *KDSR* correlates with poor outcomes in human patients with PDAC (Extended Data Fig. 4e). Together, these data suggest that inhibiting de novo sphingolipid synthesis in the cancer compartment promotes anti-tumour immunity in vivo.

Despite a significant decrease in sphingolipids (Extended Data Fig. 2b–f), SPT-deficient cells grew similarly to their SPT cDNA-expressing counterparts (Extended Data Fig. 5a) in culture and as tumours in NSG mice (Fig. 1h). Sphingolipids can be obtained from exogenous sources and metabolized in the lysosomes and other organelles into building blocks used to generate new lipids. We considered whether these cells might depend on the lysosomal salvage pathway to support their growth in culture conditions[20] when de novo synthesis is impaired. Indeed, treating *Sptlc1*-KO cells with bafilomycin-A1, a lysosomal acidification inhibitor, further depleted sphingolipid precursors and impaired proliferation, a defect that was rescued by supplementation with sphingolipid intermediates in vitro (Extended Data Fig. 5b–f). Thus, our results argue for a model in which there are two distinct thresholds of sphingolipid levels required for tumour growth: one for cell proliferation and another for immune escape. Whereas sphingolipids obtained through the salvage pathway are sufficient to sustain cell proliferation, the diversity or quantity of lipids generated via de novo synthesis may be required to achieve immune evasion.

Tumour sphingolipids dampen cytotoxic immunity

Given that sphingolipids are bioactive molecules that regulate diverse processes including cell migration, cell survival and death, and differentiation[21], we next explored how inhibition of sphingolipid synthesis in cancer cells affects immune cell composition in the TME. To address this question in an unbiased way, we performed single-cell RNA sequencing (scRNA-seq) on isolated CD45^{+} immune cells from *Sptlc1*-KO and *Sptlc1*-addback (AB) tumours grown in C57BL/6J mice. After clustering to define major tumour-infiltrating immune cell types, we found no major changes in the proportions of infiltrating lymphocytes despite alterations in those of myeloid cells in *Sptlc1*-KO tumours (Fig. 2a and Extended Data Fig. 6a,b). Further analysis revealed that NK and CD8^{+} T cells from *Sptlc1*-KO tumours exhibited upregulation of genes associated with their enhanced activation and cytotoxic states, such as interferon-γ (IFNγ), compared with those isolated from *Sptlc1*-AB tumours (Fig. 2b,c and Extended Data Fig. 6c). Flow cytometric analysis of infiltrating NK and CD8^{+} T cells confirmed their elevated activation states and higher expression of IFNγ upon loss of *Sptlc1* in tumours (Fig. 2d–f and Extended Data Fig. 6d–g). Collectively, these results suggest that sphingolipid depletion in cancer cells alters the functional state of cytotoxic lymphocytes in the TME. Consistent with this, estimates of infiltrating immune cell fractions in PDAC tumours retrieved from The Cancer Genome Atlas (TCGA) revealed a correlation between low expression of de novo sphingolipid synthesis genes (*SPTLC1*, *SPTLC2* and *KDSR*) and increased activation of NK cells (Extended Data Fig. 6h–j).

To further understand whether NK and CD8^{+} T cells are directly involved in restricting the growth of cancer cells deficient for sphingolipid synthesis, we cocultured *Sptlc1*-KO and *Sptlc1*-AB cells with NK or CD8^{+} T cells isolated from C57BL/6J or OT-1 mice, respectively. *Sptlc1*-KO cells were more sensitive to the anti-proliferative effects of NK cells, and supplementing them with 3-ketosphinganine or sphingosine was sufficient to rescue this effect (Fig. 2g). Of note, coculturing NK cells with sphingolipid-depleted or replete cancer cells induced IFNγ expression to a similar extent (Extended Data Fig. 6k–m). Similarly, CD8^{+} T cells inhibited the growth of *Sptlc1*-KO cancer cells more effectively compared with *Sptlc1*-AB controls in an antigen-specific manner (Fig. 2h and Extended Data Fig. 6n). Of note, antibody-mediated depletion of NK or CD8^{+} T cells in C57BL/6J mice significantly promoted *Sptlc1*-KO tumour growth (Extended Data Fig. 6o). Thus, these results suggest that de novo sphingolipid synthesis protects cancer cells from NK and CD8^{+} T cell immune surveillance.

Sphingolipid depletion enhances IFNγ signalling

We next sought to determine the mechanism by which cancer sphingolipids mediate immune evasion from NK and CD8^{+} T cells. Upon stimulation, NK and T cells secrete pro-inflammatory chemokines and kill target cells via the perforin–granzyme pathway, by expressing FasL or TRAIL, or producing cytokines such as IFNγ, which activate proapoptotic, pro-inflammatory and anti-proliferative signalling cascades in

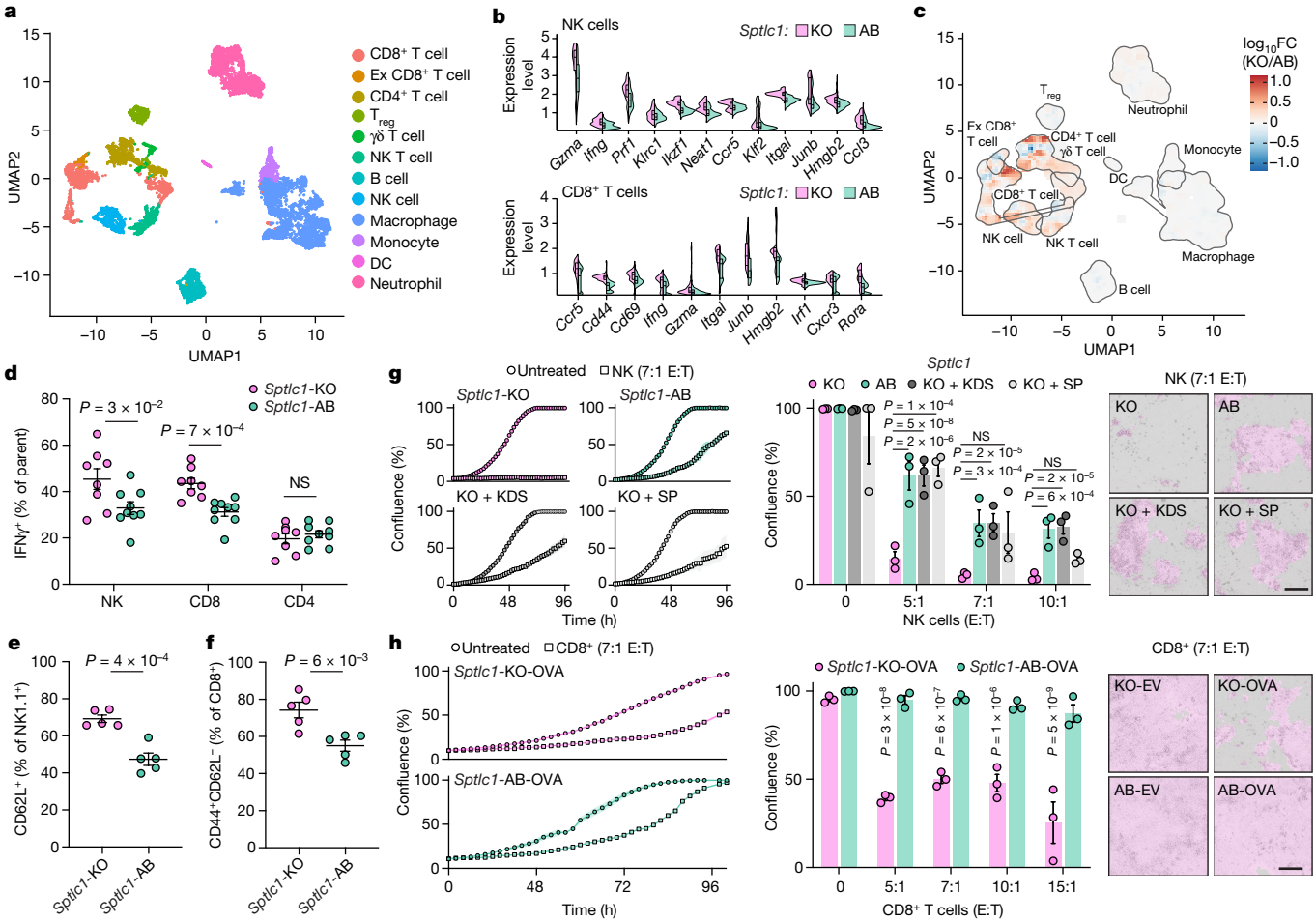

Fig. 2 | Sphingolipid synthesis protects cancer cells from the anti-tumour effects of immune cells. a, Uniform manifold approximation and projection (UMAP) plot of 17,950 CD45⁺ infiltrating leukocytes isolated from *Sptlc1*-KO or AB HY15549 tumours grown in C57BL/6J mice. DC, dendritic cell; Ex, exhausted; T_{reg}, regulatory T cell. **b**, Expression distribution of differentially expressed (adjusted *P* value < 0.0001) activation and cytotoxicity markers in NK and CD8⁺ T cells isolated from *Sptlc1*-KO or *Sptlc1*-AB HY15549 tumours grown in C57BL/6J mice. Data are mean ± s.e.m.; two-sided Wilcoxon rank-sum test with Benjamini–Hochberg correction. *n* = 5,000 cells per condition. Minima, maxima and centre bounds are defined in the source data file. **c**, FC of the average *Ifng* expression of CD45⁺ leukocytes isolated from *Sptlc1*-KO or *Sptlc1*-AB HY15549 tumours grown in C57BL/6J mice, superimposed on the UMAP shown in **a**. **d**, Flow cytometry analysis of IFNγ expression in NK cells, CD8⁺ T cells or CD4⁺ T cells isolated from *Sptlc1*-KO or *Sptlc1*-AB HY15549 tumours grown in C57BL/6J mice. Data are mean ± s.e.m.; *n* = 8 mice per group. NS, not significant. **e**, Flow cytometry analysis of the proportion of CD62L⁺ NK cells among leukocytes isolated from *Sptlc1*-KO or *Sptlc1*-AB HY15549 tumours grown in C57BL/6J mice. Data are mean ± s.e.m.; *n* = 5 mice per group. **f**, Flow cytometry analysis of the proportion of CD44⁺CD62L⁻CD8⁺ T cells among leukocytes isolated from *Sptlc1*-KO or AB HY15549 tumours grown in C57BL/6J mice. Data are mean ± s.e.m.; *n* = 5 mice per group. **g**, Left, proliferation of *Sptlc1*-KO and AB HY15549 cells supplemented with 1 μM 3-ketodihydrosphingosine (KDS) or 750 nM sphingosine (SP) left untreated or cocultured with NK cells. Middle, bar graph depicting confluence of indicated conditions at 72 h. Right, representative images of cocultured cells. Data are mean ± s.e.m.; *n* = 3 biological replicates; scale bar, 200 μm. E:T, effector:target cell ratio. **h**, Left, proliferation of ovalbumin (OVA)-expressing *Sptlc1*-KO and AB HY15549 cells left untreated or cocultured with OT-1 CD8⁺ T cells. Middle, bar graph depicting confluence of indicated conditions at 98 h. Right, representative images of the cultures. Data are mean ± s.e.m.; *n* = 3 biological replicates; scale bar, 200 μm.

target cells. Given that loss of de novo sphingolipid synthesis sensitizes cancer cells to NK and T cells in a tumour-intrinsic manner, we compared the transcriptome of *Sptlc1*-KO and *Sptlc1*-AB pancreatic cancer cells cultured in vitro or isolated from tumours grown in C57BL/6J or NSG mice (Fig. 3a and Extended Data Fig. 7a). Gene set enrichment analysis revealed that in the presence of immune surveillance, *Sptlc1*-KO cells upregulated the expression of genes involved in interferon signalling and response pathways (Fig. 3b). Coculturing *Sptlc1*-KO cells with NK cells induced similar pro-inflammatory pathways (Extended Data Fig. 7b,c), raising the possibility that loss of de novo sphingolipid synthesis may contribute to tumour cell sensitivity through interferon signalling. Interferons are cytokines that regulate cancer progression by inducing pro-inflammatory signalling in target cells and activating immune cells. IFNα and IFNβ are produced by most cell types, whereas IFNγ is primarily produced by activated NK and T cells and binds its receptor composed of IFNγ receptor subunits 1 and 2. Once interferons bind their receptor, the JAK–STAT interferon signalling pathway is activated and induces the transcription of pro-inflammatory cytokines and antigen presentation machinery in target cells. Consistent with the heightened transcriptional activation of interferon signalling, loss of sphingolipid synthesis increased phosphorylation and expression of JAK1 and STAT1 in pancreatic cancer cells upon their exposure to IFNγ or NK cells (Fig. 3c,d and Extended Data Fig. 7d,e). Moreover, genetic and pharmacological inhibition of sphingolipid synthesis sensitized HY15549 cells to IFNγ-mediated growth arrest (Fig. 3e). Conversely, overexpression of SPT blunted IFNγ-mediated growth arrest and signalling (Extended Data Fig. 7f,g). Notably, the anti-proliferative effects of IFNγ in *Sptlc1*-KO cells were rescued by CRISPR-mediated deletion

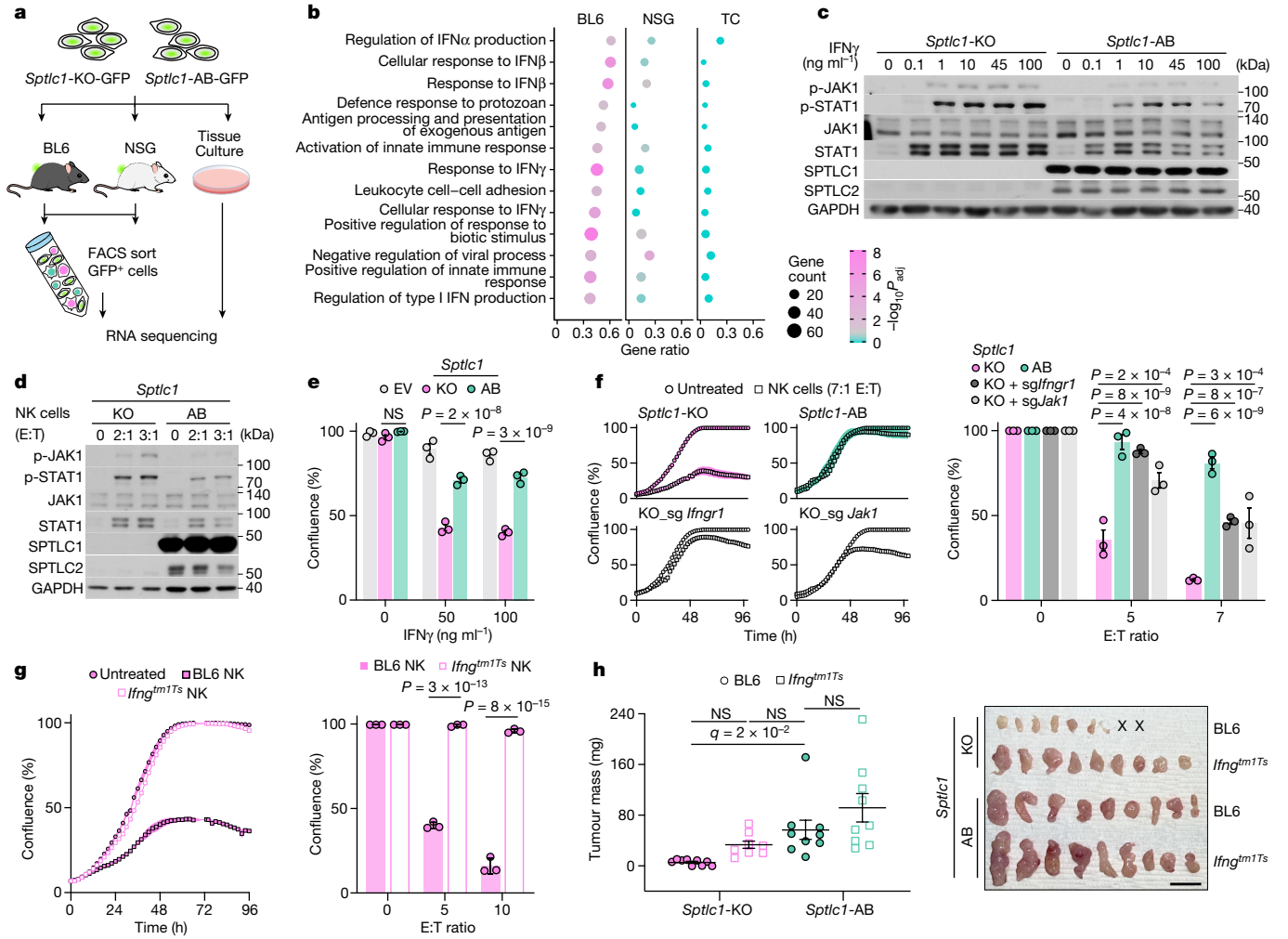

Fig. 3 | Loss of sphingolipid synthesis sensitizes cancer cells to IFNγ. a, RNA-sequencing analysis of GFP$^+$ *Sptlc1*-KO and *Sptlc1*-AB HY15549 cells grown in C57BL/6J or NSG mice. After 12 days, tumours were collected, dissociated and sorted by fluorescence-activated cell sorting (FACS) for RNA sequencing. **b**, Gene set enrichment analysis of mRNAs significantly enriched in *Sptlc1*-KO versus *Sptlc1*-AB HY15549 cells grown in C57BL/6J mice compared with those in NSG mice or cultured in vitro. TC, tissue culture. Gene Ontology (GO) terms are ranked by gene ratio, adjusted *P* values (FDR) are colour-coded, and circle size corresponds to the total number of genes in the gene set. IFN, interferon. **c**, Immunoblot showing IFNγ signalling pathway induction in *Sptlc1*-KO and *Sptlc1*-AB HY15549 cells left untreated or treated with IFNγ for 4 h. GAPDH is a loading control. **d**, Immunoblot showing IFNγ signalling pathway induction in *Sptlc1*-KO and *Sptlc1*-AB HY15549 cells cocultured with NK cells 5 h. GAPDH is a loading control. **e**, Proliferation of *Sptlc1*-KO and *Sptlc1*-AB HY15549 cells treated with the indicated concentrations of IFNγ for 92 h. Data are mean ± s.d.; $n = 3$ biological replicates. **f**, Left, proliferation of *Sptlc1*-KO, *Sptlc1*-AB, *Sptlc1*/*Ifngr1*-double knockout (KO + sg*Ifngr1*) or *Sptlc1*/*Jak1*-double knockout (KO + sg*Jak1*) HY15549 cells left untreated or cocultured with NK cells. Right, bar graph showing confluence after 72 h. Data are mean ± s.e.m.; $n = 3$ biological replicates. **g**, Left, proliferation of *Sptlc1*-KO HY15549 cells left untreated or cocultured with NK cells isolated from C57BL/6J (E:T ratio 5:1) or *Ifng*^{tm1Ts} mice (E:T ratio 5:1). Right, bar graph showing confluence after 84 h. Data are mean ± s.e.m.; $n = 3$ biological replicates. **h**, Tumour mass (left) and images (right) of *Sptlc1*-KO and *Sptlc1*-AB HY15549 tumours grown in C57BL/6J or *Ifng*^{tm1Ts} mice. Data are mean ± s.d.; $n = 3$ mice per group; scale bar, 1 cm. X indicates that tumours were not detected at the endpoint. One-way ANOVA with Benjamini–Hochberg multiple test correction.

of *Ifngr1* or *Jak1* (Fig. 3f and Extended Data Fig. 7h) and IFNγ-deficient NK cells were inefficient at restricting the growth of *Sptlc1*-KO cells in culture (Fig. 3g). Finally, the anti-tumour effects of *Sptlc1* loss were partially abrogated in IFNγ-deficient (*Ifng*^{tm1Ts}) mice, suggesting that tumour sphingolipids protect cancer cells against host IFNγ signalling (Fig. 3h).

Glycosphingolipids affect membrane IFNGR1

Given that changes in membrane lipid composition may influence the properties of membrane proteins[22], we next sought to determine whether loss of sphingolipid synthesis affects the function or expression of specific membrane proteins. To address this, we performed parallel proteomic analyses on whole-cell and plasma membrane proteins isolated from *Sptlc1*-KO and *Sptlc1*-AB pancreatic cancer cells (Fig. 4a and Extended Data Fig. 8a,b). Although loss of *Sptlc1* did not induce profound changes in the proteome of whole cells (Extended Data Fig. 8c), we observed substantial alterations in the abundance of membrane proteins of *Sptlc1*-KO cells compared with *Sptlc1*-AB controls (Fig. 4b). In particular, IFNGR1 was among the membrane proteins upregulated in *Sptlc1*-KO cells, in addition to proteins involved in receptor-mediated endocytosis (such as AP2M1, EPS15 and CUBN). These results are consistent with previous work showing that IFNGR partitions into membrane lipid nanodomains upon activation and impairment of this redistribution blocks the internalization of IFNGR[23,24]. We therefore tested whether loss of sphingolipid synthesis may sensitize cells to IFNγ by disrupting IFNGR1 surface expression. Immunoblot and flow cytometric analysis of *Sptlc1*-KO and AB cells revealed a higher

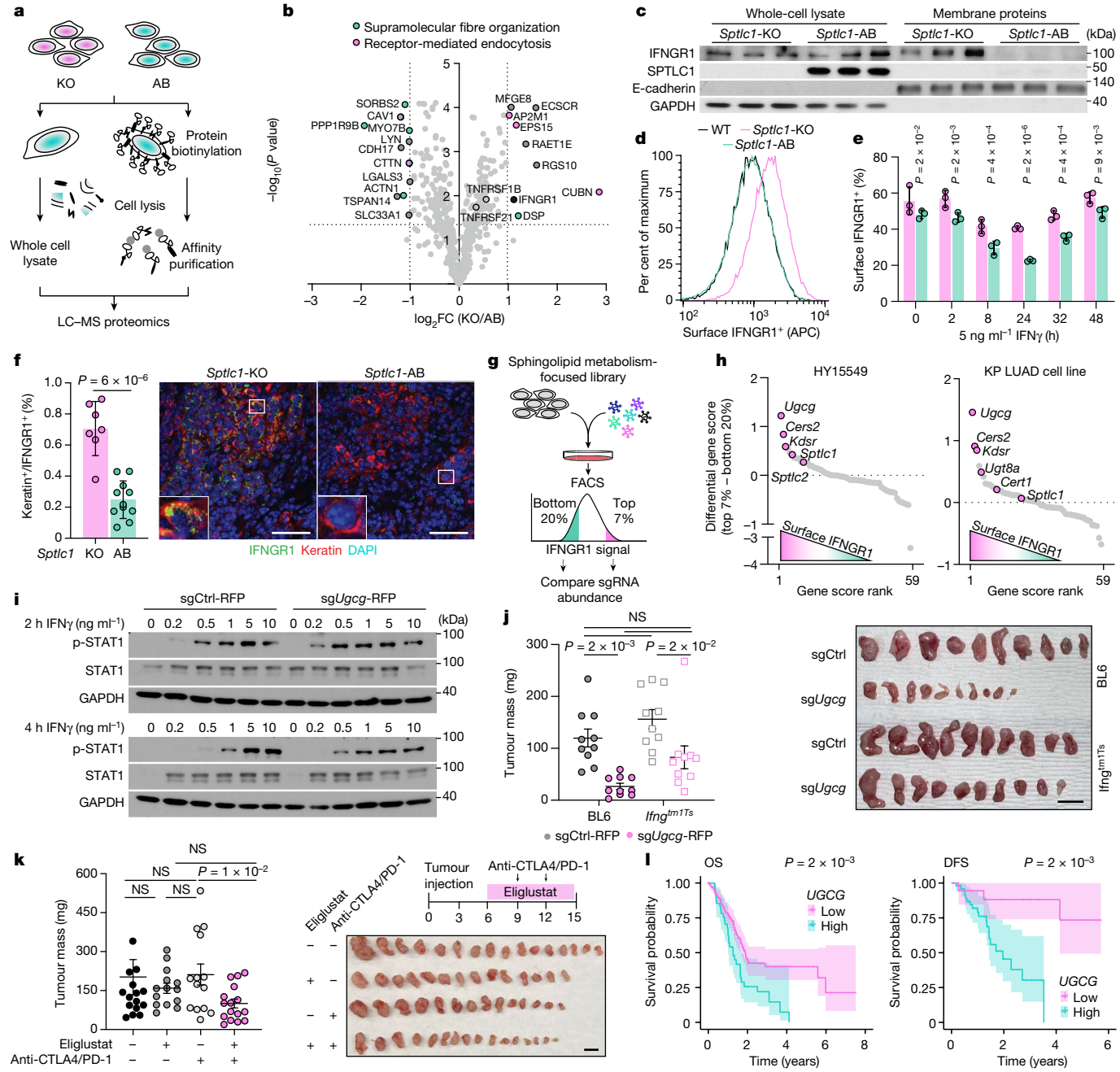

Fig. 4 | Glycosphingolipid synthesis affects cell surface expression of IFNGR1. a, *Sptlc1*-KO and *Sptlc1*-AB HY15549 cells untreated or incubated with a membrane-impermeable biotin tag. Cells were lysed and labelled proteins were affinity purified. Eluted protein and unlabelled whole-cell protein lysates were analysed by liquid chromatography–mass spectrometry (LC–MS). **b**, The $\log_2$-transformed fold change in whole-cell and membrane proteins between *Sptlc1*-KO (KO) versus *Sptlc1*-AB (AB) HY15549 cells. **c**, Immunoblot of whole-cell and membrane protein lysates from *Sptlc1*-KO and *Sptlc1*-AB HY15549 cells. $n = 3$ biological replicates. **d**, Flow cytometry analysis of IFNGR1 surface expression in wild-type, *Sptlc1*-KO and *Sptlc1*-AB HY15549 cells. APC, allophycocyanin. **e**, Flow cytometry analysis of IFNGR1 surface expression in *Sptlc1*-KO and *Sptlc1*-AB HY15549 cells treated with 5 ng ml^{-1} IFNγ over time. Data are mean ± s.e.m.; $n = 3$ biological replicates. **f**, Quantification of the number of IFNGR1$^+$keratin$^+$ cells in *Sptlc1*-KO ($n = 2$) and *Sptlc1*-AB ($n = 3$) HY15549 tumours grown in C57BL/6J mice for 12 days. Data are mean ± s.e.m.; $n = 3$ images per tumour. Scale bars, 50 µm. **g**, FACS-based screen to identify sphingolipid metabolism genes that affect the stability of IFNGR1 in the plasma membrane of HY15549 and KP LUAD cells. Live transduced cells were incubated with a fluorescent antibody against IFNGR1. High- and low-fluorescence populations were collected, and the amount of sgRNA was compared. **h**, Ranks of differential gene scores between IFNGR1^{hi} and IFNGR1^{low} HY15549 and KP LUAD cells. De novo glycosphingolipid pathway genes among the top 20 scoring genes are highlighted. **i**, Immunoblot of IFNγ signalling pathway induction in sgCtrl-RFP and sg*Ugcg*-RFP HY15549 cells untreated or treated with IFNγ for 2 or 4 h. **j**, Tumour mass (left) and images (right) of sgCtrl-RFP and sg*Ugcg*-RFP HY15549 tumours grown in C57BL/6J or *Ifng*^{tm1Ts} mice. Data are mean ± s.e.m.; $n = 5$ mice per group; scale bar, 1 cm. One-way ANOVA with Tukey's multiple test correction. **k**, Tumour mass and image of wild-type HY15549 tumours grown in C57BL/6J mice treated as indicated. Data are mean ± s.e.m.; $n = 7$ (no treatment or eliglustat plus anti-CTLA4/PD-1) or 8 (eliglustat only or anti-CTLA4/PD-1) mice per group; scale bar, 1 cm. One-way ANOVA with Tukey's multiple test correction. **l**, Survival analysis of patients with PDAC from TCGA data with high or low expression of *SPTLC1*, *SPTLC2* and *KDSR*. $n = 177$. Data are mean ± 95% confidence interval. DFS, disease-free survival; OS, overall survival.

abundance of IFNGR1 surface expression in sphingolipid-depleted cells (Fig. 4c–e and Extended Data Fig. 8d,e). Notably, this difference was sustained upon IFNγ stimulation and correlated with increased sensitivity to IFNγ signalling (Extended Data Fig. 8f). These results were confirmed by immunofluorescence experiments (Extended Data Fig. 8g–i). Furthermore, analysis of tissue samples from *Sptlc1*-KO and *Sptlc1*-AB tumours grown in C57BL/6J mice showed that loss of sphingolipid synthesis significantly increased IFNGR1 expression in vivo (Fig. 4f).

To determine which ceramide-derived lipid species affect IFNGR1 levels in the plasma membrane, we conducted a FACS-based genetic screen for membrane IFNGR1 expression using a sphingolipid metabolism-focused CRISPR library in HY15549 and KP LUAD cells (Fig. 4g). Among the top scoring genes was UDP-glucose ceramide glucosyltransferase (*Ugcg*), which catalyses the first committed step in the conversion of ceramides to glycosphingolipids (Fig. 4h). By contrast, genes involved in sphingomyelin, ceramide-1-phosphate or sphingosine-1-phosphate synthesis did not score (Extended Data Fig. 9a), indicating that glycosphingolipid synthesis has a role in mediating IFNGR1 surface expression. Confirming this, loss of *Ugcg* resulted in significant depletion of glycosphingolipids and their precursors and significantly increased the levels of plasma membrane IFNGR1 (Extended Data Fig. 9b–f). Additionally, glycosphingolipid depletion increased sensitivity to IFNγ and impaired tumour growth in immunocompetent, but not immunocompromised mice (Fig. 4i and Extended Data Fig. 9g,h). The anti-tumour effects of UGCG loss were partially abrogated in IFNγ-deficient mice, suggesting that glycosphingolipids partly protect cancer cells against IFNγ-mediated tumour control (Fig. 4j). Whereas these results suggest a connection between glycosphingolipids and membrane expression of IFNGR1, it should be noted that the availability of sphingolipids in the plasma membrane affects the localization and function of a number of other membrane proteins[22]. For example, disruption of lipid nanodomain formation upon SPTLC1 loss correlates with impaired VEGF signalling in endothelial cells[25]. Similarly, we observed changes in the abundance of other immune receptors in the membrane proteome of SPTLC1-deficient cells, including enrichment of TNF receptor subunits (Fig. 4b).

Glycosphingolipid loss enhances immunotherapy

We next sought to determine whether targeting glycosphingolipid synthesis could enhance tumoral responses to immune therapy. Eliglustat, a small molecule inhibitor of UGCG, is a well-tolerated clinical drug that is used to reduce lipid accumulation in Gaucher disease, a lysosomal storage disorder[26]. Pharmacological inhibition of UGCG with eliglustat depleted glycosphingolipids and their precursors in cultured HY15549 cells and increased sensitivity to IFNγ-induced growth arrest in both HY15549 and KP LUAD cells (Extended Data Fig. 10a–d). To test whether pharmacological depletion of glycosphingolipids sensitizes KRAS-driven tumours to immunotherapy, we treated HY15549 or KP LUAD tumour-bearing immunocompetent mice with a combination of eliglustat and checkpoint blockade therapy (CBT). Notably, whereas dual CBT with anti-CTLA4 and anti-PD-1 (anti-CTLA4/PD-1) did not impair HY15549 tumour growth, eliglustat treatment synergized with dual CBT to significantly reduce tumour burden (Fig. 4k). Similarly, eliglustat treatment synergized with anti-PD-1 CBT to reduce KP LUAD tumour growth (Extended Data Fig. 10e). Tumour burden was not significantly affected by eliglustat treatment alone, probably owing to incomplete target engagement or effects on other cell types in the TME, including immune cells. Finally, consistent with the role of glycosphingolipid synthesis in human cancers, querying the TCGA-PanCanAtlas dataset revealed a significant correlation between high expression of *UGCG* and disease severity in patients with PDAC (Fig. 4l and Extended Data Fig. 10f).

Discussion

Alterations in sphingolipid metabolism have been described in tumours since the 1970s[27,28]. Our work reveals glycosphingolipid availability as a critical endogenous limitation for immune evasion in KRAS-driven cancer cells. Of note, increased glycolytic flux into glycosphingolipid synthesis promotes the plasma membrane localization of oncogenic KRAS, which reciprocally upregulates glycosphingolipid synthesis[29]. Additionally, glycosphingolipids and UGCG expression were recently shown to be upregulated in response to inhibition of lysosomal autophagy[30], a critical process involved in immune evasion of *KRAS*-mutant tumours[31–34]. The convergence of multiple immune evasion pathways on glycosphingolipid availability may suggest that KRAS-driven tumours may be particularly vulnerable to immune surveillance upon glycosphingolipid depletion. Recent systematic in vivo CRISPR screens showed that sphingolipid synthesis is not a universal essentiality for tumour growth[35]. Future work will determine whether this strategy is restricted to *KRAS*-mutant tumours or can be generalized to other cancer types.

Here we show that glycosphingolipid synthesis promotes immune evasion by affecting surface expression of IFNGR1, in line with the major role of IFNγ signalling in immune surveillance and immunotherapy efficacy[36,37]. IFNGR1 has recently been suggested to directly bind sphingolipids upon IFNγ stimulation[38], raising the possibility that direct lipid–protein interactions may regulate its stability in the plasma membrane. Given that expression of sphingolipid synthesis enzymes is often upregulated in a wide range of tumour types[28] and that pharmacological inhibition of glycosphingolipid synthesis synergizes with immune CBT in tumour models, whether an increase in membrane glycosphingolipids predicts cancer progression and response to immunotherapy in patients should be studied. Increased serum levels of sphingomyelins and glycosphingolipids predict cancer disease progression and patients with Gaucher disease accumulate glycosphingolipids and have an increased risk of developing cancer[39]. Thus, altering membrane sphingolipid composition pharmacologically or via dietary interventions could be a viable strategy to improve immunotherapy response. Finally, our screens reveal that other membrane lipids, such as phosphatidylcholines and phosphatidylethanolamines may also affect tumour immune escape. Further research is needed to understand how cancer cells leverage membrane phospholipids to promote growth in different tumour types and physiological contexts.

Online content

Any methods, additional references, Nature Portfolio reporting summaries, source data, extended data, supplementary information, acknowledgements, peer review information; details of author contributions and competing interests; and statements of data and code availability are available at https://doi.org/10.1038/s41586-024-07787-1.

1. Ubellacker, J. M. et al. Lymph protects metastasizing melanoma cells from ferroptosis. *Nature* **585**, 113–118 (2020).
2. Young, R. M. et al. Dysregulated mTORC1 renders cells critically dependent on desaturated lipids for survival under tumor-like stress. *Genes Dev.* **27**, 1115–1131 (2013).
3. Ackerman, D. et al. Triglycerides promote lipid homeostasis during hypoxic stress by balancing fatty acid saturation. *Cell Rep.* **24**, 2596–2605.e5 (2018).
4. Harayama, T. & Riezman, H. Understanding the diversity of membrane lipid composition. *Nat. Rev. Mol. Cell Biol.* **19**, 281–296 (2018).
5. Wymann, M. P. & Schneiter, R. Lipid signalling in disease. *Nat. Rev. Mol. Cell Biol.* **9**, 162–176 (2008).
6. Snaebjornsson, M. T., Janaki-Raman, S. & Schulze, A. Greasing the wheels of the cancer machine: the role of lipid metabolism in cancer. *Cell Metab.* **31**, 62–76 (2020).
7. Kamphorst, J. J. et al. Hypoxic and Ras-transformed cells support growth by scavenging unsaturated fatty acids from lysophospholipids. *Proc. Natl Acad. Sci. USA* **110**, 8882–8887 (2013).
8. Beyaz, S. et al. High-fat diet enhances stemness and tumorigenicity of intestinal progenitors. *Nature* **531**, 53–58 (2016).
9. Broadfield, L. A. et al. Fat induces glucose metabolism in nontransformed liver cells and promotes liver tumorigenesis. *Cancer Res.* **81**, 1988–2001 (2021).

10. Pascual, G. et al. Dietary palmitic acid promotes a prometastatic memory via Schwann cells. *Nature* **599**, 485–490 (2021).
11. Altea-Marzano, P. et al. A palmitate-rich metastatic niche enables metastasis growth via p65 acetylation resulting in pro-metastatic NF-κB signaling. *Nat. Cancer* **4**, 344–364 (2023).
12. Ringel, A. E. et al. Obesity shapes metabolism in the tumor microenvironment to suppress anti-tumor immunity. *Cell* **183**, 1848–1866.e26 (2020).
13. Martin-Perez, M., Urdiroz-Urricelqui, U., Bigas, C. & Benitah, S. A. The role of lipids in cancer progression and metastasis. *Cell Metab.* **34**, 1675–1699 (2022).
14. Beyaz, S. et al. Dietary suppression of MHC class II expression in intestinal epithelial cells enhances intestinal tumorigenesis. *Cell Stem Cell* **28**, 1922–1935.e5 (2021).
15. Xu, S. et al. Uptake of oxidized lipids by the scavenger receptor CD36 promotes lipid peroxidation and dysfunction in $CD8^+$ T cells in tumors. *Immunity* **54**, 1561–1577.e7 (2021).
16. Ogretmen, B. Sphingolipid metabolism in cancer signalling and therapy. *Nat. Rev. Cancer* **18**, 33–50 (2018).
17. Hannun, Y. A. & Obeid, L. M. Sphingolipids and their metabolism in physiology and disease. *Nat. Rev. Mol. Cell Biol.* **19**, 175–191 (2018).
18. Gault, C., Obeid, L. & Hannun, Y. in *Sphingolipids as Signaling and Regulatory Molecules* (eds Chalfant, C. & Del Poeta, M.) 1–23 (Springer, 2010).
19. Codini, M., Garcia-Gil, M. & Albi, E. Cholesterol and sphingolipid enriched lipid rafts as therapeutic targets in cancer. *Int. J. Mol. Sci.* **22**, 726 (2021).
20. Unlu, G. et al. Metabolic-scale gene activation screens identify SLCO2B1 as a heme transporter that enhances cellular iron availability. *Mol. Cell* **82**, 2832–2843.e7 (2022).
21. Maceyka, M. & Spiegel, S. Sphingolipid metabolites in inflammatory disease. *Nature* **510**, 58–67 (2014).
22. Corradi, V. et al. Emerging diversity in lipid–protein interactions. *Chem. Rev.* **119**, 5775–5848 (2019).
23. Marchetti, M. et al. Stat-mediated signaling induced by type I and type II interferons (IFNs) is differentially controlled through lipid microdomain association and clathrin-dependent endocytosis of IFN receptors. *Mol. Biol. Cell* **17**, 2896–2909 (2006).
24. Blouin, C. M. & Lamaze, C. Interferon gamma receptor: the beginning of the journey. *Front. Immunol.* **4**, 267 (2013).
25. Kuo, A. et al. Murine endothelial serine palmitoyltransferase 1 (SPTLC1) is required for vascular development and systemic sphingolipid homeostasis. *eLife* **11**, e78861 (2022).
26. Lukina, E. et al. Outcomes after 8 years of eliglustat therapy for Gaucher disease type 1: final results from the phase 2 trial. *Am. J. Hematol.* **94**, 29–38 (2019).
27. Gahmberg, C. G. & Hakomori, S. I. Altered growth behavior of malignant cells associated with changes in externally labeled glycoprotein and glycolipid. *Proc. Natl Acad. Sci. USA* **70**, 3329–3333 (1973).
28. Ryland, L. K., Fox, T. E., Liu, X., Loughran, T. P. & Kester, M. Dysregulation of sphingolipid metabolism in cancer. *Cancer Biol. Ther.* **11**, 138–149 (2011).
29. Liu, J. et al. Glycolysis regulates KRAS plasma membrane localization and function through defined glycosphingolipids. *Nat. Commun.* **14**, 465 (2023).
30. Jain, V. et al. Targeting UGCG overcomes resistance to lysosomal autophagy inhibition. *Cancer Discov.* **13**, 454–473 (2023).
31. Commisso, C. et al. Macropinocytosis of protein is an amino acid supply route in Ras-transformed cells. *Nature* **497**, 633–637 (2013).
32. Perera, R. M. et al. Transcriptional control of the autophagy-lysosome system in pancreatic cancer. *Nature* **524**, 361–365 (2015).
33. Zhu, X. G. et al. Functional genomics in vivo reveal metabolic dependencies of pancreatic cancer cells. *Cell Metab.* **33**, 211–221.e6 (2021).
34. Yamamoto, K. et al. Autophagy promotes immune evasion of pancreatic cancer by degrading MHC-I. *Nature* **581**, 100–105 (2020).
35. Dubrot, J. et al. In vivo CRISPR screens reveal the landscape of immune evasion pathways across cancer. *Nat. Immunol.* **23**, 1495–1506 (2022).
36. Lawson, K. A. et al. Functional genomic landscape of cancer-intrinsic evasion of killing by T cells. *Nature* **586**, 120–126 (2020).
37. Larson, R. C. et al. CAR T cell killing requires the IFNγR pathway in solid but not liquid tumours. *Nature* **604**, 563–570 (2022).
38. Contreras, F.-X. et al. Molecular recognition of a single sphingolipid species by a protein's transmembrane domain. *Nature* **481**, 525–529 (2012).
39. Dubot, P. et al. Are glucosylceramide-related sphingolipids involved in the increased risk for cancer in Gaucher disease patients? Review and hypotheses. *Cancers* **12**, 475 (2020).

Methods

Reagents

Recombinant mouse interferons were purchased from BioLegend: IFNγ (581302). The following reagents were purchased from Cayman Chemical Company: Myriocin (63150), 3-ketosphinganine (24380), C2-ceramide (62510), C6-ceramide (62525), sphingosine (10007907) and sphingosine-1-phosphate (62570).

Animal studies

All mouse experiments were conducted in accordance with a protocol approved by the Institutional Animal Care and Use Committee at The Rockefeller University. C57BL/6J (000664), NSG (005557), B6.129S7-*Rag1*^{tm1Mom}/J (002216), B6.129S7-*Ifng*^{tm1Ts}/J (002287), C57BL/6-Tg(TcraTcrb)1100Mjb/J (003831) were obtained from The Jackson Laboratory. All mice were maintained on a standard light–dark cycle with food and water ad libitum. Mice were euthanized before tumours reached the maximum volume of 2 cm^3 and before mice showed any signs of distress (ruffled fur, extensive weight loss, poor body condition or poor grooming related to debilitation).

Cell lines and cell culture

HY15549 cells were obtained from N. M. Bardeesy and are originally derived from female KPC mice that were backcrossed into a C57BL/6 background[40], KP LUAD cells were obtained from T. Papagiannakopoulos. Cell lines were regularly checked for *Mycoplasma* contamination and were grown in RPMI 1640 medium (Gibco 11875-093) containing 2 mM glutamine supplemented with 10% fetal bovine serum (FBS) (Sigma-Aldrich 12306 C) and 1% penicillin/streptomycin (Gibco 15140-122). Cells were maintained at 37 °C, 21% O_2 and 5% CO_2.

In vivo CRISPR screens

For the lipid metabolism-focused screen, a list of 295 genes was curated based on previous metabolism-focused screens and literature review. Seven sgRNAs per gene were included in the library along with 40 non-targeting sgRNA controls. The library was cloned into lentiCRISPRv2-Opti puro (Addgene 163126) and used to make virus-containing supernatant as described above. HY15549 cells (2.5 million) were infected as above at a multiplicity of infection (MOI) of ~0.7 and selected with puromycin. Following selection, an initial pool of 2.5 million cells was collected for genomic DNA extraction. Transduced cells were prepared for subcutaneous injection at a concentration of 1 million cells per 100 µl in 30% Matrigel (R&D Systems BME001-5). Each mouse received one 100 µl injection subcutaneously on each flank. Myeloablation was achieved by exposing C57BL/6J mice to 5.5 Gy radiation 48 h prior to tumour injections. Depletion of immune cells was confirmed at day 0 and day 18 by determining blood counts on an ElementHT5 (Heska). After 18 days, the tumours were collected and their genomic DNA extracted using a DNeasy Blood & Tissue Kit (Qiagen). For each mouse, genomic DNA from each tumour was pooled equally and sgRNA inserts were amplified by PCR using unique barcoding primers per mouse. sgRNA abundance was measured by sequencing (NextSeq 500, Illumina). The gene score for each gene was defined as median $\log_2$ fold change in abundance of each sgRNA targeting that gene. The gene score across mice within each group was averaged.

KEGG pathway analysis was performed on the top 60 commonly essential genes between C57BL/6J mice versus myeloablated C57BL/6J or NSG mice using ShinyGO[41] (v.0.76.3). Top enriched pathways were selected from the top 50 most significant *P* values, pathways comprised of more than 300 genes were excluded and scoring pathways were ranked by fold enrichment.

For the ceramide metabolism-focused screen, a list of 59 genes was curated from the sphingolipid metabolism pathway defined by Kegg (00600) with modifications based on literature review. At least 4 sgRNAs and gene and 40 non-targeting sgRNA controls were included in the library. The library was cloned into lentiCRISPRv2-Opti puro (Addgene 163126) and used to make virus-containing supernatant as described above. One million cells were infected as above at an MOI of ~0.7 and selected with puromycin. Following selection, an initial pool of 1 million cells was collected for genomic DNA extraction. KP LUAD cells were prepared at 300,000 cells per 100 µl in 30% Matrigel. Each mouse (C57BL/6J, NSG, $n = 4–5$ per group) received one 100 µl injection subcutaneously on each flank. Genomic DNA extraction, PCR amplification and quantification of sgRNAs, and gene score analysis was performed as above.

FACS-based CRISPR screen

HY15549 or KP LUAD cells (2.5 million) were infected as above at an MOI of ~0.7 and selected with puromycin. Following selection, an initial pool of 2.5 million cells was collected for genomic DNA extraction and transduced cells were expanded for another 48 h. Sixty million cells were collected and washed once with PBS. Cells were resuspended in 50 µl FACS buffer (PBS, 1% BSA, 5 mM EDTA) containing 1:10 antibody (Miltenyi Biotec 130-104-935)/ million cells and incubated in the dark at 4 °C for 15 min. To wash cells, 10 ml FACS buffer was added to each sample before centrifugation at 500*g* for 5 min at 4 °C. Pellets were resuspended in FACS buffer with DAPI and the top 7% and bottom 20% fluorescent cells were sorted and collected using a Sony MA900. Genomic DNA extraction, PCR amplification and quantification of sgRNAs, and gene score analysis was performed as above.

Generation of knockout, addback and overexpression cell lines

sgRNA sequences (listed below) were synthesized by IDT and cloned with T4 ligase (NEB) into lentiCRISPRv2-puro (Addgene 982990) (*Sptlc1*, *Sptlc2* and *Ugcg*_sg5), lentiCRISPRv1-GFP (Addgene 75159) *(Ifngr1* and *Jak1*) or lentiCRISPRv1-RFP (Addgene 75162) (sgCtrl, *Ugcg*_sg4) linearized with BsmBI (NEB). Knockdown was confirmed by western blot except for *Ugcg*-KO, which were verified using ICE analysis (Synthego, Supplementary Information). Guide-resistant cDNAs (*Sptlc1*: NM_009269.2, *Sptlc2*: NM_011479.4) were codon-optimized, synthesized by Twist Biosciences and cloned using Gibson Assembly (NEB) into pMXS-IRES-BLAST (Cell Biolabs RTV-016) or pMXS-IRES-GFP (Cell Biolabs RTV-013) linearized with BamHI and NotI. shRNA were cloned into pLKO.1 (Addgene 10878). For lentiviral virus production, sgRNA-expressing vectors and packaging vectors (VSV-G and Delta-VPR) were transfected into HEK 293T cells using XtremeGene 9 transfection reagent (Roche). For retroviral virus production, cDNA expressing vectors and packaging vectors (VSV-G and Gag-Pol) were transfected into HEK 293T cells using XtremeGene 9 transfection reagent (Roche). Virus-containing supernatant was collected 48 h after transfection and passed through a 0.45-µm filter. Eighteen hours prior to infection, target cells (30,000–50,000 cells per well) were plated in a 6-well plate. Cells were spin-infected with 300–500 µl of virus and 4 µg ml^{-1} polybrene by centrifugation at 2,200 rpm for 80 min. Twenty-four hours after infection, medium was refreshed. Forty-eight hours after infection, cells were selected by puromycin (lentiCRISPRv2-puro), blasticidin (pMXS-IRES-BLAST), or FACS (lentiCRISPRv1-GFP). *Sptlc1*-KO and *Sptlc2*-KO cells were single-cell cloned. All clonal cell lines were compared to their addback counterparts. For all infections, the matching vector without insert was used as the control. A list of sgRNA and shRNA oligonucleotides can be found in Supplementary Table 1.

Immunoblotting

After washing once with PBS, cells were lysed on ice for 10 min in RIPA buffer (10 mM Tris-HCl pH 7.5, 150 mM NaCl, 1 mM EDTA, 1% Triton X-100, 0.1% SDS) containing protease inhibitors (Roche 490685001). Lysates were centrifuged at 4 °C for 10 min at 14,000 rpm. Twenty

micrograms of protein per sample were resolved on 12%, 4–12% or 10–20% Tris-Glycine gels (Invitrogen XP00125BOX, XP04125BOX and XP10205BOX). Gels were transferred in CAPS buffer (10 mM CAPS, 10% ethanol) to PVDF membranes (EMD Millipore 1PVH00010) which were then blocked in 5% BSA at room temperature for 1 h and incubated with primary antibodies at 4 °C overnight: GAPDH (GeneTex GTX627408), SPTLC1 (Proteintech 15376-1-AP) SPTLC2 (Proteintech 51012-2-AP), IFNGR1 (Proteintech 10808-1-AP), p-STAT1 (R&D Systems AF2894-SP), STAT1 (Cell Signaling Technology 14994T), JAK1 (Cell Signaling Technology 3344S), p-JAK1 (Cell Signaling Technology 3331S), e-Cadherin (Cell Signaling Technology 14472S), β-actin (GeneTex GTX109639) and CAV1 (Cell Signaling Technologies 3238S). After 3× 5-min washes in TBST (0.1% Tween-20 Tris-buffered saline) membranes were incubated with secondary antibody (anti-mouse IgG–HRP, CST 7076 or anti-rabbit IgG–HRP, CST 7074, diluted 1:5,000) at room temperature for 1 h. After 3× 5-minute washes in TBST, membranes were developed using ECL chemiluminescence (Perkin Elmer NEL105001EA or Cytiva RPN2232). For gel source data, see Supplementary Fig. 1.

Lipid extraction and profiling

For lipidomic analysis of ceramide-derived lipid species, 500,000 cells were kept on ice and washed 3 times with ice-cold saline. Cells were quenched with 667 µl of ice-cold methanol per well, scraped and collected. For tumour samples, 10 mg of tissue were homogenized in 667 µl of methanol using a Bead Ruptor (Omni). Ice-cold chloroform (333 µl) was added to the cell lysate and tissue homogenate followed by incubation on a heat block (2,000 rpm) at 48 °C for 30 min. Samples were centrifuged for 10 min at maximum speed and the supernatant transferred to a new tube. Methanolic KOH (50 µl × 1 M) was added to each sample prior to incubation on a shaking heat block (2,000 rpm) at 37 °C for 2 h. The mixture was neutralized with 2 µl of glacial acetic acid followed by centrifugation for 10 min at maximum speed (4 °C). The supernatant transferred to a new tube, dried under nitrogen, and stored at −80 °C until LC–MS analysis was performed.

Dried lipid extracts were reconstituted in 30–50 µl of 65:30:5 acetonitrile:isopropanol:water (v/v/v), vortexed for 20 s, centrifuged for 30 min (20,000*g*, 4 °C) and 5 µl of the supernatant was injected into the LC–MS in a randomized order, with separate injections for positive and negative ionization modes. Lipid extracts were separated on an Ascentis Express C18 2.1 mm × 150 mm × 2.7 µm particle size column and analysed with a Q Exactive benchtop orbitrap mass spectrometer (Thermo Fisher Scientific), as described[42].

The mass spectrometer was operated with the following parameters: spray voltage, ±3,500 V; heated capillary temperature, 320 °C; sheath gas, 60 a.u.; auxiliary gas, 20 a.u. External mass calibration was performed every 3–4 days using the standard calibration mixture. Mass spectra were acquired, in both positive and negative ionization modes, using a Top15 data-dependent MS/MS method. The full MS scan was acquired as such; 70,000 resolution, 1×10^6 AGC target, 250 ms maximum injection time, scan range 200–2,000 *m*/*z*. The data-dependent MS/MS scans were acquired at a resolution of 17,500 AGC target of 1×10^5, 75 ms maximum injection time, 1.0 Da isolation width, stepwise normalized collision energy of 10 (+), 20 (+/−), 30 (+/−), 40 (+/−) units and 8 s dynamic exclusion.

High-throughput identification and relative quantification of lipids was performed using LipidSearch software (v.4.2.27, Thermo Fisher Scientific/Mitsui Knowledge Industries) and the default parameters for Q Exactive product search and alignment. The aligned Lipid Ion report was exported to Microsoft Excel and the lipid ions were filtered down to one main adduct/ lipid using an in-house script. These lipids were then filtered using the following criteria: 'Rej' (Reject parameter calculated by LipidSearch) equal to 0; 'PQ' (peak quality parameter calculated by LipidSearch software) greater than 0.75; 'Grade' threshold of A–C (Grade is calculated by LipidSearch software but the specific threshold is dependent on the lipid class and mass spec parameters); mnain lipid adduct must be a relevant/common ion for a specific lipid class (predetermined with standards); background noise <10–15%. Lipid ion data were further curated using retention time indexing and the filtered dataset was normalized to the total cholesterol content/ sample. All lipidomics results are included in the Supplementary Information.

Cell proliferation experiments

For cell counting experiments, cells were plated in triplicate at a concentration of 1,000 cells per well in 6-well plates. On days 2, 4 and 6 after plating, each well was resuspended and counted. For proliferation experiments in in 96-well plates, cells were plated in triplicate at a concentration of 500 cells per well with indicated treatments. For proliferation experiments using Cell Titer Glo (Promega) (bafilomycin-A1 treatment experiments) an initial time point of untreated cells was used for normalization. After 4 days of growth, 40 µl of Cell Titer Glo reagent was added to each well and luminescence was read using a SpectraMax M3 plate reader (Molecular Devices). For Incucyte (Sartorius) proliferation experiments (myriocin, IFNγ and IFNβ treatment experiments), wells were imaged every 2 h for up to 5 days.

Tumour experiments

For shRNA-expressing, mixed population and KO and AB cells, 1 million cells in 100 µl of serum free DMEM with 30% Matrigel were injected subcutaneously into the flanks of mice. For SPT dEV and dOE cells, 0.25 million cells in 100 µl of serum free DMEM with 30% Matrigel were injected subcutaneously into the flanks of mice. For NK and $CD8^+$ T cell depletion, tumour-bearing mice were treated with an 200 µg intraperitoneal injection of every third day starting the day of tumour injection.

For eliglustat and checkpoint blockade synergy experiments, 300,000 wild-type HY15549 or 250,000 KP LUAD wild-type cells in 100 µl of serum free DMEM with 30% Matrigel were injected subcutaneously into the flanks of mice. Groups of mice were randomly assigned to the different treatment groups and treatment regimens are described in the corresponding figures. For eliglustat-treated mice, eliglustat hemitartrate (BOC Sciences B2693-474918; Selleckchem S4433) was diluted in sterile blood bank saline and administered via intraperitoneal injection at a dose of 65 mg kg^{-1} in 100 µl. Mice receiving immunotherapy were treated with 200 µg of anti-CTLA4 (9H10) (HY15549; Bio X Cell BE0131) or anti-PD-1 (29 F.1A12) (KP LUAD; Bio X Cell BE0273). Tumour volume was measured using a caliper and calculated as (length × $width^2$)/2.

For orthotopic pancreas injections, 500,000 cells in 100 µl of serum free DMEM with 50% Matrigel were injected into the pancreatic tail of anaesthetized mice using insulin syringes (29-gauge needle, BD). The peritoneum was closed with a 3-0 Vicryl Violet suture (Ethicon), and the skin was closed using the BD AutoClip Wound Closing System (BD). Mice were euthanized and tumours were dissected after 2 weeks.

Hydrodynamic tail vein injections

pT3-Kras-IRES-Luc-U6-sgRNA vector was generated by cloning $Kras^{G12D}$ cDNA coupled to IRES-Luciferase sequence under EF1a promoter; additionally cloning U6 promoter upstream of sgRNA cloning and scaffold sequence. Control or *Sptlc1*-targeting sgRNA (sequences below) were cloned into pT3. Plasmid mix containing 6.5 µg of pT3-Kras-IRES-Luc-U6-sgRNA, 1.3 µg of pCMV-SB13 transposase, and 25 µg of pX330 expressing Cas9 cDNA along with p53 sgRNA were prepared in sterile 0.9% NaCl solution. Six-week-old female mice were injected through the lateral tail vein with a volume of plasmid/saline mix corresponding to 10% of body weight within 5–7 s as described previously[43,44]. Taking advantage of luciferase signal, tumour progression was monitored weekly by IVIS. Total luminescence flux was measured by IVIS and plotted to compare tumour progression in control and *Spltc1*-KO tumours. sgRNA sequences: sg*Tp53*, CCTCGAGCTCCC TCTGAGCC; sgCtrl: GTGGGAACAGAGATAAGAAG; *Sptlc1*_sg6: AGGAAG AACTGATTGAAGAG.

Immune cell isolation and expansion

The spleen (and inguinal lymph nodes for OT-1 $CD8^+$ T cell isolation) of C57BL/6J, B6.129S7-*Ifng*^{tm1Ts}/J (*Ifng*-KO), or C57BL/6-Tg (TcraTcrb)1100Mjb/J (OT-1) mice were collected and dissociated on a 35-mm plate over ice using a scalpel. The tissue was resuspended in cold MACS buffer (PBS, 0.5% BSA and 2 mM EDTA) and passed through a 70-µm cell strainer. The plunger of a 3-ml syringe was used to push remaining tissue through the strainer, which was then rinsed with MACS buffer. Cells were centrifuged at room temperature for 6 min at 1,000 rpm. RBC lysis was performed by incubating cells in ACK lysis buffer (Thermo Scientific A1049201) at room temperature for 4 min. An equal volume of MACS buffer was added to the cell suspension and transferred through a 70-µm cell strainer into a new tube. Cells were centrifuged again at room temperature for 6 min at 1,000 rpm, resuspended in 1 ml of MACS buffer, and counted. NK and $CD8^+$ T cells were isolated from the cell suspension using negative selection isolation kits following the manufacturer's protocols (Miltenyi Biotec 130-115-818 and 130-104-075, respectively). NK cells were immediately used for coculture assays. $CD8^+$ T cells were cultured for 6-7 days at a concentration of 10^6 cells per ml in T cell medium (RPMI 1640 medium, 2 mM glutamine, 1 mM pyruvate, 10% FBS, 1% penicillin/streptomycin, 1× MEM amino acids (Thermo Scientific 11130051), 50 µM mercaptoethanol, pH ~7.4) with 20 ng ml^{-1} IL-2. T cell activation was performed by culturing cells with anti-CD3/CD28 Dynabeads (Thermo Fisher Scientific 11456D) at a beads:cell ratio of 1:2.

Immune cell–cancer cell coculture assays

To allow adherence, HY15549 were plated in triplicate at a concentration of 1,000 cells per 100 µl per well in a 96-well plate 18 h before the addition of NK cells. After NK cells were isolated, they were resuspended in T cell medium supplemented with 1 ng ml^{-1} IL-15 (R&D Systems 447-ML), 20 ng ml^{-1} IL-2 (BioLegend 575404), and 20 ng ml^{-1} IL-12 (R&D Systems 419-ML-010). One-hundred microlitres of NK cells were added at the respective E:T ratios for each well. For $CD8^+$ T cell coculture assays, HY15549 cells were plated in triplicate at a concentration of 1,000 cells per 100 µl per well in a 96-well plate with 5 ng ml^{-1} IFNγ. One-hundred microlitres of T cells was immediately added to cancer cells at the respective E:T ratios. HY15549 cell death and proliferation was monitored over 4–5 days using Incucyte.

Membrane protein biotinylation and isolation

HY15549 cells were plated 18 h prior to the addition of IFNγ so that they would reach 80% confluency on the day of collection. After respective incubation times, all samples were collected at the same time. All steps were performed on ice or at 4 °C. Cells were washed 3 times with 10 ml ice-cold PBS. Ten millilitres of 20 mM EZ-Link Sulfo-NHS-LC-Biotin (Thermo Scientific 21335) was added to the cells. Plates were incubated at 4 °C for 30 min. Plates were washed once with 10 ml ice-cold TBS (pH 7.4) and then twice with ice-cold PBS. Cells were then scraped off the plate, collected, and centrifuged at 500*g* for 5 min at 4 °C. Cells were resuspended in RIPA buffer containing protease inhibitors and incubated on ice for 30 min. Lysates were sonicated for 5 min and then centrifuged at maximum speed for 10 min at 4 °C. Lysates were transferred to streptavidin beads (Thermo Scientific 88816) and incubated on a rotor at 4 °C for 1 h. Beads were briefly spun down, magnetized, and washed 3 times with 1 ml of PBS. Protein was eluted off of the beads by resuspending them in 50–100 µl of transmembrane buffer (10 mM Tris-HCl pH 7.4, 1 mM EDTA, 1% Triton X-100, 2% SDS, 0.1% CHAPS) with 1× SDS loading buffer (20% SDS) and boiling samples for 5 min at 95 °C. Beads were then magnetized and the lysate collected.

Proteomics

Cysteines were reduced and alkylated with dithiothreitol and iodoacetamide. Proteins were precipitated with ice-cold acetone and the pellet was dissolved in 200 mM EPPs containing 1 µg trypsin. Digestion proceeded overnight at room temperature, at which point 1 µg of trypsin was added and temperature was increased to 50 °C for 1 h. Peptides were labelled with TMTpro, quenched with hydroxylamine and, once stoichiometry was verified, pooled. TMTpro peptides were separated into 8 fractions by high-pH reversed-phase spin columns and analysed by LC–MS/MS using an Easy nLC 1200 HPLC equipped with a 250 mm × 75 µm Easyspray column connected to an orbitrap Fusion Lumos mass spectrometer operating in positive DDA mode.

Spectra were queried against the *Mus musculus* proteome (database downloaded from https://www.uniprot.org/ on 22 September 2020) at 1% FDR using the Sequest HT search engine through Proteome Discoverer v. 2.5 and a spectral purity of 75% was required for quantitation. Protein abundance values were further processed within the Perseus statistical software environment.

Flow cytometry analysis of IFNGR1 and membrane glycosphingolipids

Cells (500,000) were collected and washed once with PBS. For extracellular staining, cells were resuspended in 50 µl FACS buffer containing 1:10 antibody (Miltenyi Biotec 130-104-935) and incubated in the dark at 4 °C for 15 min. To wash cells, 1 ml of FACS buffer (PBS, 1% BSA, 5 mM EDTA) was added to each sample before centrifugation at 500*g* for 5 min at 4 °C. Pellets were resuspended in FACS buffer with DAPI and immediately analysed on an Attune NxT (Thermo Scientific). For intracellular staining, 500,000 cells were collected and washed once with PBS. To fix and permeabilize the cells, samples were resuspended in 50 µl of PBS and 200 µl of 100% ice-cold methanol was added dropwise while gently vortexing. Cells were incubated in 80% methanol on ice for 20 min. Then, 1 ml of PBS was added, and cells centrifuged at 500*g* for 5 min at 4 °C. IFNGR1 staining and acquiring proceeded as above.

For analysis of membrane glycosphingolipids, 500,000 cells were collected and washed once with PBS. Cells were resuspended in 50 µl FACS buffer containing 1:100 cholera toxin B-AF647 (Invitrogen C34778) and incubated in the dark at 4 °C for 20 min. Cells were washed with PBS and resuspended in flow buffer containing DAPI. Samples were acquired as above. An example of the gating strategies used for these experiments is included in the Supplementary Information.

Flow cytometry analysis of tumour-infiltrating immune cells

Tumours were excised and digested for 1 h at 37 °C with with 400 U ml^{-1} of collagenase D (Roche) and 0.2 µg ml^{-1} DNase I (Sigma). Digested tumours were filtered through 70-µm filters. Enrichment of haematopoietic cells was achieved by density gradient centrifugation with 40%/90% Percoll (GE Healthcare Life Sciences) for 25 min at 2,500 rpm at 22 °C without breaks. The interphase containing haematopoietic cells was isolated and washed with phosphate-buffered EDTA (PBE). Red blood cell lysis was performed with ACK lysis buffer (GIBCO). For cytokine staining, cells were incubated at 37 °C for 4 h in complete RPMI medium supplemented with brefeldin A (Sigma), phorbol 12-myristate 13-acetate (PMA) (Sigma) and ionomycin (Sigma). Following incubation, cells were washed with PBE. Cells were incubated for 5 min with 1 µg ml^{-1} of anti-CD16/32 (2.4G2, BioXcell) at room temperature. Cells were washed with PBS and stained with Zombie fixable viability dye (Biolegend) for 15 min at room temperature. Cells were washed with PBE and stained with appropriate surface marker antibodies for $CD4^+$ and $CD8^+$ T cells and NK cells for 20 min at 4 °C. Cells were washed with PBE, fixed, and permeabilized (Cytofix/Cytoperm kit, BD). Intracellular staining for IFNγ was performed for 30 min at 4 °C. Cells were washed and resuspended in PBE. Samples were acquired on a BD FACSymphony and data were analysed using FlowJo v.10.6.2 software.

Flow cytometry analysis of IFNγ in NK cells

Twenty thousand GFP-expressing target cells were plated in each well of a round bottom 96-well plate. NK cells were isolated as above

and added to target cells at a 3:1 ratio in the presence of IL-15, IL-2 and IL-12. After an overnight incubation, each well was treated with brefeldin A (BioLegend 420601) for 4 h. After, NK cells were collected, washed and permeabilized using the BD Cytofix/Cytoperm kit (BD BioSciences 554714) following the manufacturer's instructions. NK cells were stained on ice for 20 min with primary antibody (1:200, Thermo Scientific 17-7311-81). Samples were acquired using Attune NxT (Thermo Scientific).

Tumour dissociation, cell isolation and RNA sequencing

Tumours were removed from mice 12–13 days after injection and placed into DMEM$^+$ medium (DMEM/F-12 Gibco 11320033, 10% FBS) and kept on ice. Once all tumours were removed, they were washed once with ice-cold PBS and placed into a 1.5-ml tube containing dissociation buffer (DMEM$^+$, 1 mg ml^{-1} Collagenase D (Sigma-Aldrich 11088858001), 25 μg ml^{-1} DNAse (NEB M0303S)). Tumours were briefly dissociated using scissors and then incubated on a shaking heat block for 35 min at 37 °C. Each sample was then passed through a 70-μm cell strainer which was rinsed with 5 ml DMEM$^+$. Cell suspensions were centrifuged at 300*g* for 5 min at 4 °C. Cells were resuspended in 3 ml ACK buffer and incubated at room temperature for 4 min. Then, 7 ml DMEM$^+$ was added before centrifuging again at 300*g* for 5 min at 4 °C.

For bulk RNA sequencing of GFP-expressing tumour cells, cells were resuspended in FACS buffer with DAPI. GFP-positive/DAPI-negative cells (70–100,000) were sorted into Trizol LS (Fisher Scientific 10-296-010). Total RNA was extracted using chloroform and sequenced using Illumina NextSeq.

For isolation of CD45$^+$ tumour-infiltrating immune cells, cells were resuspended in 30 μl of FACS buffer containing Fc-block (1:200, BD BioSciences 553141) and incubated on ice for 10 min. 30 μl of CD45 antibody in FACS buffer was added to cells (1:10 final concentration) and incubated on ice for 20 min. Cells were washed by adding 1 ml FACS buffer prior to centrifugation at 1,000*g* for 5 min at 4 °C. Cells were resuspended in 200 μl of DAPI-containing FACS buffer. Ten thousand CD45$^+$DAPI$^-$ cells per mouse were sorted into a pre-coated Eppendorf tube for a total of 60,000 cells per condition. Five thousand cells per condition were targeted for scRNA-seq on a Chromium Single Cell System (10x Genomics). Samples were processed per the manufacturer's instructions (Chromium single cell 3′ reagents, v3.1 chemistry) and libraries were sequenced using Illumina NovaSeq.

For RNA sequencing of cells cocultured with NK cells in vitro HY15549 cells were plated in triplicate at 100,000 cells per well in a 6-well plate 18 h prior to the addition of NK cells. Freshly isolated NK cells were added at an E:T ratio of 2:1 and incubated together for 6 h. Then, the medium was aspirated and adherent cells were thoroughly washed three times with PBS to remove remaining NK cells. HY15549 cells were collected in PBS, pelleted, and snap frozen prior to RNA extraction using chloroform. RNA was sequenced using Illumina NextSeq.

Bulk RNA-sequencing analysis

Sequence and transcript coordinates for the mouse genome (mm10 UCSC) and gene models were retrieved from the Bsgenome.Hsapiens.UCSC.mm10 (v1.4.0) and TxDb.Hsapiens.UCSC.mm10.knownGene (v3.4.0) Bioconductor libraries, respectively. Transcript expression was calculated using Salmon quantification software[45] (v0.8.2) and gene expression levels were expressed as transcripts per million (TPM). Normalization and rlog transformation of raw read counts in genes were performed using DESeq2[46] (v1.20.0). Genes significantly differentially expressed between conditions were identified using DESeq2 with a Benjamini–Hochberg adjusted *P* value cutoff of 0.05. Gene Ontology of analyses of significantly differentially expressed genes was done using AmiGO 2[47] and the GO Biological Process pathway database. Dot plots were simplified by excluding gene sets comprised of more than 200 genes.

scRNA-seq analysis

Single-cell datasets for each experiment were independently assessed for data quality following the guidelines described[48,49]. Cells with more than 10% mitochondrial transcripts as well as cells that had fewer than 250 feature counts or expressed fewer than 500 genes were removed. After quality control, Seurat (v4.0.3) was used for normalization, graph-based clustering and differential expression analysis[50]. Each dataset was normalized using SCTransform and the 5000 most variable genes were identified with SelectIntegrationFeatures. Both empty vector control cells and addback (AB) datasets were integrated into a singular dataset via using the PrepSCTIntegration, FindIntegrationAnchors, and IntegrateData function[51]. MAGIC imputation was conducted on integrated data to impute missing values and account for technical noise[52,53]. RunPCA was implemented on the integrated datasets to identify the top 50 principal components that were used for UMAP analysis and clustering. Louvain clustering at a resolution of 1 was implemented. Clusters were labelled in accordance with expression levels of CD45 tumour-infiltrating lymphocyte subtype signatures. Differential expression analysis was conducted between empty vector control cells versus addback cells using the FindMarkers function with the MAST method to evaluate differences within the transcriptome[54]. Wilcoxon rank-sum tests to determine if gene expression was significant was conducted using the wilcox.test function in stats (v4.1.0). For the density map of the differential expression of *Ifng*, cells were binned based on proximity in the UMAP. Log fold change of *Ifng* expression (knockout versus addback) was calculated using the cells in each bin and transposed back onto the UMAP at the generalized location of the cells.

Immunofluorescence

For immunocytochemistry on HY15549 cells, 100,000 cells were seeded on poly-D-lysine coated coverslips in 6-well plates and grown overnight. After the indicated treatments, cells were washed twice with PBS and incubated at room temperature with cholera toxin B-AF647 conjugate (Invitrogen C34778) diluted in PBS for 10 min. Cells were then washed with PBS and fixed in 4% paraformaldehyde for 20 min at room temperature. Fixation was followed by 3× 5-min washes in PBS prior to mild permeabilization with 0.1% Triton X-100 for 10 min at room temperature and another round of 3× 5-min PBS washes. Coverslips were blocked in 1% BSA for 1 h at room temperature and incubated in anti-IFNGR1 antibody (1:200, Invitrogen PA5-27841) diluted in 1% BSA overnight at 4 °C. After 3× 5-min PBS washes, coverslips were incubated with secondary antibody in 1% BSA (1:250, Invitrogen A-21428) and anti-caveolin CoraLite588 conjugate (1:200, Proteintech CL488-66067) for 1 h at room temperature. Cells were washed once with PBS for 10 min, then incubated for 10 min with DAPI. Coverslips were then rinsed with water and mounted (Invitrogen P36934). Slides were imaged with Nikon A1R MP multiphoton microscope with confocal modality, using Nikon Plan Apo γ 60×/1.40 oil immersion objective. Images were processed and analysed with FIJI (ImageJ2, v2.3.0.1).

For immunofluorescence staining on formalin-fixed paraffin embedded tissue sections of HY15549 tumours grown subcutaneously in syngeneic mice, tissue was fixed overnight in 10% formalin at room temperature and subsequently stored in 70% ethanol. Tissue was embedded in paraffin and 10 μm sections were cut. Sections were deparaffinized and rehydrated in xylene and ethanol. Antigen retrieval was performed in Tris-EDTA Buffer (10 mM Tris, 1 mM EDTA, 0.05% Tween-20) for 10 min in a pressure cooker on low pressure. Tumour sections were blocked with SuperBlock (Thermo Fisher) for 2 h at room temperature, after which sections were incubated with a primary polyclonal antibody against IFNGR1 (1:500, Thermo Fisher, PA5-27841) in PBS with 1% BSA overnight at 4 °C. Sections were washed 3 times using PBS with 0.05% Tween-20. Subsequently, sections were exposed to Alexa Fluor 488 conjugated anti-rabbit antibody (1:500, Thermo Fisher, A32790) for 1 h at room temperature, followed by primary antibody against pan-keratin

(1:250, Cell Signaling Technology, 4545T) overnight at 4 °C, and Alexa Fluor 647 conjugated anti-mouse antibody (1:500, Thermo Fisher, A31573) for 1 h at room temperature with intermittent washing steps. Finally, DAPI solution (0.5 μg ml^{-1}, Thermo Fisher, 62248) was applied to the section and stained at room temperature for 10 min. Samples were imaged on a Zeiss LSM 710 laser scanning confocal microscope, using a Plan-Apochromat 40×/1.3 Oil DIC M27 Oil immersion lens. Images were processed with FIJI (ImageJ2, Version 2.3.0). After *z*-projection and brightness/contrast adjustment, image quantification was manually performed in QuPath[55] with surface pan-keratin staining identifying pan-keratin positive cells and IFNGR1 intensity of 1000 or higher identifying IFNGR1-positive cells.

Survival analysis of TCGA data

TPM-normalized RNA-sequencing count matrices for 177 PDAC tumours from the TCGA pan-cancer dataset[56] were retrieved using the cBio Cancer Genomics Portal[57]. Genes with a coefficient of variation >0.25 were selected and *z*-score normalized across samples. Expression scores for each sample were calculated by the average *z*-score of genes in a gene set. Samples were classified into high-expression and low-expression groups based on their respective, thresholded expression scores. Survival analysis was conducted for the TCGA PDAC tumours using the *coxph* function from the survival R package while controlling for tumour TNM (tumour, node and metastasis) stage, sex, age, grade and radiation therapy status. One-hundred and seventy seven PDAC tumours were classified into high- and low-expressing tumours using the surv_cutpoint() function from the survminer[58] R package, which determines the optimal cut point using the maximally selected rank statistic from the 'maxstat' R package[59].

Statistical analysis

Each experiment was repeated independently at least twice with similar results. Data were analysed by unpaired, two-sided Student's *t*-test unless otherwise specified in the figure legend.

Analysis of tumour-infiltrating leukocytes in PDAC patient samples from TCGA

Relative fractions of immune cell types for each PDAC tumour, estimated using CIBERSORT[60], were retrieved from TCGA[61]. For a given immune cell type, 177 PDAC tumours were classified into high and low-expressing tumours by iteratively testing thresholds in the interquartile range of a gene set's *z*-score using an unpaired two-sided Student's *t*-test. Thresholds within the interquartile range that maximized the *t*-statistic were selected.

Reporting summary

Further information on research design is available in the Nature Portfolio Reporting Summary linked to this article.

Data availability

Proteomics data have been deposited to the ProteomeXchange Consortium with the dataset identifier PXD052718. scRNA-seq data has been deposited to the NCBI Gene Expression Omnibus and can be accessed with the accession number GSE270660. Source data are provided with this paper.

40. Bardeesy, N. et al. Both p16Ink4a and the p19Arf-p53 pathway constrain progression of pancreatic adenocarcinoma in the mouse. *Proc. Natl Acad. Sci. USA* **103**, 5947–5952 (2006).
41. Ge, S. X., Jung, D. & Yao, R. ShinyGO: a graphical gene-set enrichment tool for animals and plants. *Bioinformatics* **36**, 2628–2629 (2020).
42. Soula, M. et al. Metabolic determinants of cancer cell sensitivity to canonical ferroptosis inducers. *Nat. Chem. Biol.* **16**, 1351–1360 (2020).
43. Xue, W. et al. CRISPR-mediated direct mutation of cancer genes in the mouse liver. *Nature* **514**, 380–384 (2014).
44. Huang, C.-H. et al. CDK9-mediated transcription elongation is required for MYC addiction in hepatocellular carcinoma. *Genes Dev.* **28**, 1800–1814 (2014).
45. Patro, R., Duggal, G., Love, M. I., Irizarry, R. A. & Kingsford, C. Salmon provides fast and bias-aware quantification of transcript expression. *Nat. Methods* **14**, 417–419 (2017).
46. Love, M. I., Huber, W. & Anders, S. Moderated estimation of fold change and dispersion for RNA-seq data with DESeq2. *Genome Biol.* **15**, 550 (2014).
47. Carbon, S. et al. AmiGO: online access to ontology and annotation data. *Bioinformatics* **25**, 288–289 (2009).
48. Luecken, M. D. & Theis, F. J. Current best practices in single-cell RNA-seq analysis: a tutorial. *Mol. Syst. Biol.* **15**, e8746 (2019).
49. Amezquita, R. A. et al. Orchestrating single-cell analysis with Bioconductor. *Nat. Methods* **17**, 137–145 (2020).
50. Butler, A., Hoffman, P., Smibert, P., Papalexi, E. & Satija, R. Integrating single-cell transcriptomic data across different conditions, technologies, and species. *Nat. Biotechnol.* **36**, 411–420 (2018).
51. Stuart, T. et al. Comprehensive integration of single-cell data. *Cell* **177**, 1888–1902.e21 (2019).
52. van Dijk, D. et al. Recovering gene interactions from single-cell data using data diffusion. *Cell* **174**, 716–729.e27 (2018).
53. Zheng, L. et al. Pan-cancer single-cell landscape of tumor-infiltrating T cells. *Science* **374**, eabe6474 (2021).
54. Finak, G. et al. MAST: a flexible statistical framework for assessing transcriptional changes and characterizing heterogeneity in single-cell RNA sequencing data. *Genome Biol.* **16**, 278 (2015).
55. Bankhead, P. et al. QuPath: open source software for digital pathology image analysis. *Sci. Rep.* **7**, 16878 (2017).
56. The Cancer Genome Atlas Consortium. *The Pan-Cancer Atlas* http://www.cell.com/pb-assets/consortium/pancanceratlas/pancani3/index.html (Cell Press, 2018).
57. Cerami, E. et al. The cBio Cancer Genomics Portal: an open platform for exploring multidimensional cancer genomics data. *Cancer Discov.* **2**, 401–404 (2012).
58. Kassambara, A., Kosinski, M., Biecek, P. & Fabian, S. survminer: Drawing survival curves using 'ggplot2'. https://CRAN.R-project.org/package=survminer (2021).
59. Hothorn, T. maxstat: Maximally selected rank statistics. https://CRAN.R-project.org/package=maxstat (2017).
60. Newman, A. M. et al. Robust enumeration of cell subsets from tissue expression profiles. *Nat. Methods* **12**, 453–457 (2015).
61. Thorsson, V. et al. The immune landscape of cancer. *Immunity* **48**, 812–830.e14 (2018).

Acknowledgements The authors thank all Birsoy laboratory members for their thoughtful suggestions; members of the Rockefeller University Genomics Resource Center, Proteomics Resource Center and the Flow Cytometry Resource Center for their assistance. M.S. is a Howard Hughes Medical Institute (HHMI) Gilliam Fellow. G.U. is a Damon Runyon Fellow supported by the Damon Runyon Cancer Research Foundation (DRG-2431-21). We thank Cold Spring Harbor Laboratory (CSHL) Cancer Center Imaging Core Facility supported by NCI Cancer Center Support grant 5P30CA045508. S.B. acknowledges funding from The Oliver S. and Jennie R. Donaldson Charitable Trust, The G. Harold and Leila Y. Mathers Foundation, STARR Cancer Consortium (I13-0052) and The Mark Foundation for Cancer Research (20-028-EDV). K.B. is supported by the NIH/NIDDK (R01 DK123323-01), NIH/NCI (5U54CA261701-03), the Reem-Kayden award, Black Family Metastasis Research Center and Mark Foundation Emerging Leader Award. Data were generated by the Proteomics Resource Center at The Rockefeller University (RRID:SCR_017797) using instrumentation funded by the Sohn Conferences Foundation and the Leona M. and Harry B. Helmsley Charitable Trust.

Author contributions K.B. and M.S. conceived of the project, designed the experiments, and wrote the manuscript with input from S.B. M.S. performed most of the experiments. G.U. helped with IFNγ sensitivity, proliferation and subcutaneous tumour experiments, and performed the hydrodynamic tail vein injections and luciferase flux assays. B.U. and R.W. helped with the in vivo CRISPR screens and coculture assays. A.C. performed flow cytometric immune profiling experiments. V. Shah performed the scRNA-seq analysis. H.A. performed the lipidomic analyses. P.B. performed tissue staining and analysis of IFNGR1 expression in tumours. V. Subramanyam performed survival and CIBERSORT analyses. H.-W.Y. performed orthotopic pancreas tumour injections. A.K. helped with bulk RNA-seq analysis. S.H. performed proteomic analyses. H.G. and G.D.V. provided input.

Competing interests K.B. is a scientific advisor to Nanocare Pharmaceuticals and Atavistik Bio. M.S. is an employee of Lime Therapeutics. The other authors declare no competing interests.

Additional information

Supplementary information The online version contains supplementary material available at https://doi.org/10.1038/s41586-024-07787-1.

Correspondence and requests for materials should be addressed to Kıvanç Birsoy.

Peer review information *Nature* thanks the anonymous reviewer(s) for their contribution to the peer review of this work. Peer reviewer reports are available.

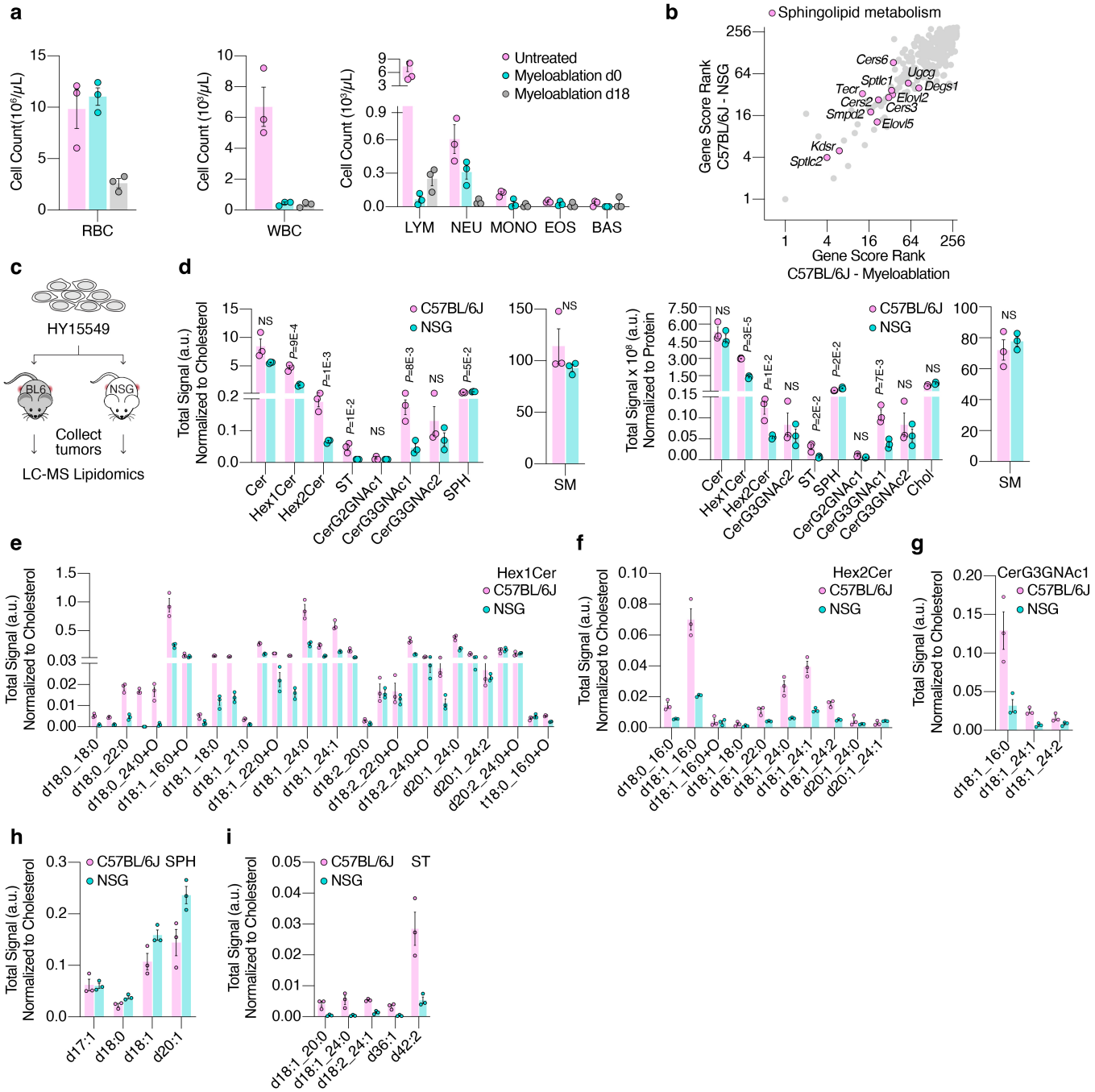

Extended Data Fig. 1 | Cancer cell sphingolipid availability mediates immune evasion. a. Cell count of red blood cells (RBC, left), white blood cells (WBC, middle), lymphocytes (LYM, right), neutrophils (NEU), monocytes (MONO), eosinophils (EOS), and basophils (BAS) in untreated C57BL/6 J mice (pink) and myeolablated C57BL/6 J mice on the day of tumor injections (d0, 36 h after radiation) and at the endpoint (d18). Mean ± SEM; n = 3 mice/ group. b. Ranks of differential gene scores between C57BL/6 J and myeloablated mice (x-axis) or NSG mice (y-axis). The highlighted genes are among the top 60 scoring genes and are involved in sphingolipid biosynthesis. c. Schematic of wildtype HY15549 cells grown in C57BL/6 J or NSG mice for 12 days before tumor collection and lipid extraction. Lipid abundances were determined by LC-MS analysis (right). d. Abundance of ceramide-derived lipid species in HY15549 cells grown in C57CBL/6 J versus NSG mice. Lipid abundance is normalized to cholesterol levels (left) or to total protein (right). Mean ± SEM, n = 3 mice/ group. e. Abundance of hexosyl-1-ceramides in HY15549 cells grown in C57CBL/6 J versus NSG mice. Lipid abundance is normalized to cholesterol levels. Mean ± SEM, n = 3 mice/ group. f. Abundance of hexosyl-2-ceramides in HY15549 cells grown in C57CBL/6 J versus NSG mice. Lipid abundance is normalized to cholesterol levels. Mean ± SEM, n = 3 mice/ group. g. Abundance of glucosylceramides in HY15549 cells grown in C57CBL/6 J versus NSG mice. Lipid abundance is normalized to cholesterol levels. Mean ± SEM, n = 3 mice/ group. h. Abundance of sphingosines in HY15549 cells grown in C57CBL/6 J versus NSG mice. Lipid abundance is normalized to cholesterol levels. Mean ± SEM, n = 3 mice/ group. i. Abundance of sulfatides in HY15549 cells grown in C57CBL/6 J versus NSG mice. Lipid abundance is normalized to cholesterol levels. Mean ± SEM, n = 3 mice/ group.

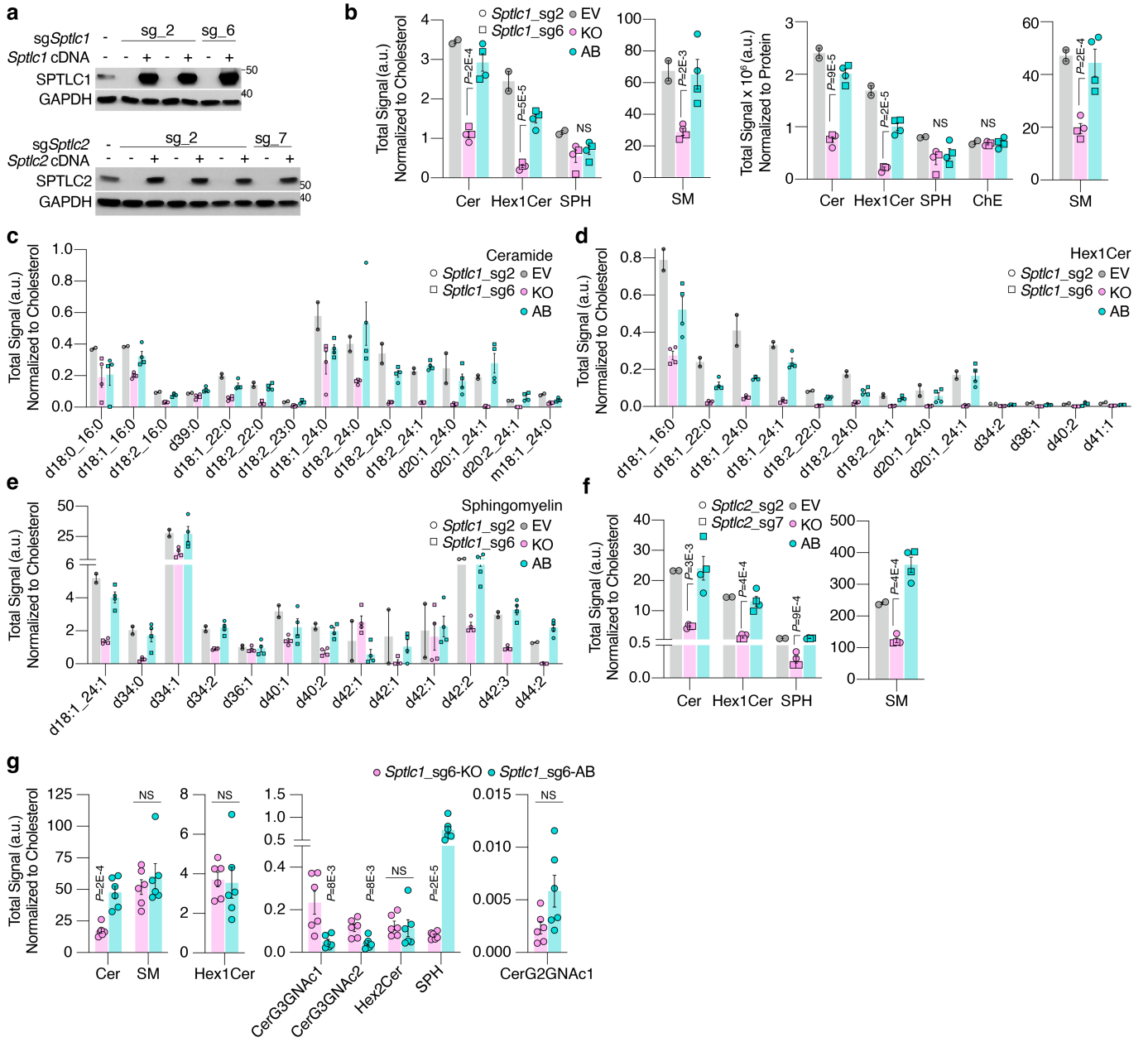

Extended Data Fig. 2 | Loss of *Sptlc1* or *Sptlc2* depletes ceramide-derived lipid species. a. Immunoblot analysis of SPTLC1 (top) and SPTLC2 (bottom) expression in wildtype HY15549 cells or knockout and cDNA-expressing clonal pairs. GAPDH is used as a loading control. b. Abundance of ceramide-derived lipid species in empty vector parental, *Sptlc1*-KO (KO) and *Sptlc1*-AB (AB) HY15549 cells. Abundance is normalized to cholesterol levels of each sample (left) or to protein (right). Mean ± SEM, n = 2 biological replicates/ cell line. c. Abundance of ceramide species in empty vector parental, *Sptlc1*-KO (KO) and *Sptlc1*-AB (AB) HY15549 cells. Abundance is normalized to cholesterol levels of each sample. Mean ± SEM, n = 2 biological replicates/ cell line. d. Abundance of hexosyl-1-ceramide species in empty vector parental, *Sptlc1*-KO (KO) and *Sptlc1*-AB (AB) HY15549 cells. Abundance is normalized to cholesterol levels of each sample. Mean ± SEM, n = 2 biological replicates/ cell line. e. Abundance of sphingomyelin species in empty vector parental, *Sptlc1*-KO (KO) and *Sptlc1*-AB (AB) HY15549 cells. Abundance is normalized to cholesterol levels of each sample. Mean ± SEM, n = 2 biological replicates/ cell line. f. Abundance of ceramide-derived lipid species in empty vector parental, *Sptlc2*-KO (KO) and *Sptlc2*-AB (AB, blue) HY15549 cells. Abundance is normalized to cholesterol levels of each sample. Mean ± SEM, n = 2 biological replicates/ cell line. g. Abundance of ceramide-derived lipid species in *Sptlc1*-KO (KO) and *Sptlc1*-AB (AB) HY15549 cells grown as tumors in C57BL/6 J mice for 12 days. Abundance is normalized to cholesterol levels of each sample (left) or to protein (right). Mean ± SEM, n = 2 biological replicates/ cell line.

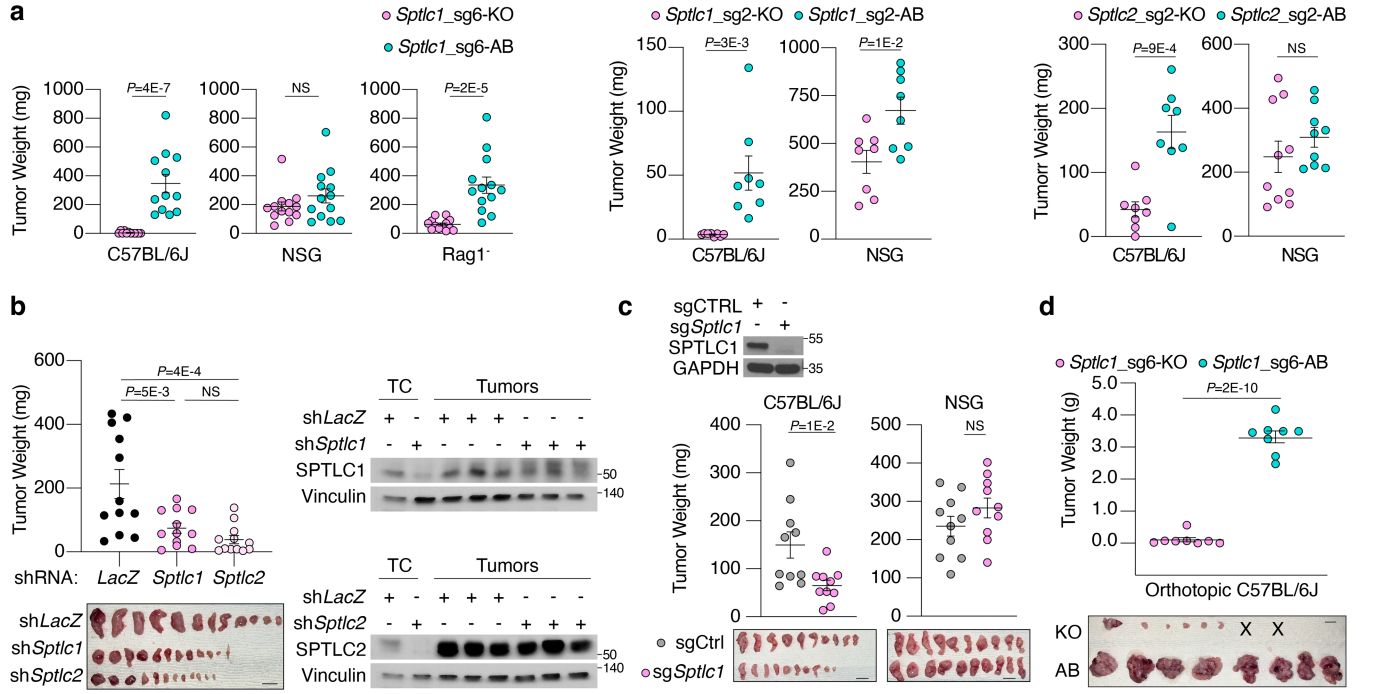

Extended Data Fig. 3 | Loss of SPT impairs tumor growth in immunocompetent mice. a. Weights of *Sptlc1*_sg6-KO (KO, pink) and *Sptlc1*_sg6-AB (AB, blue) HY15549 tumors grown in C57BL/6 J, NSG, or Rag^{-} mice corresponding to Fig. 1g (left). Weights of *Sptlc1*_sg2-KO (KO, pink) and *Sptlc1*_sg2-AB (AB, blue) HY15549 tumors grown in C57BL/6 J or NSG mice (middle). Weights of *Sptlc2*_sg2-KO (KO, pink) and *Sptlc2*_sg2-AB (AB, blue) HY15549 tumors grown in C57BL/6 J or NSG mice (right). Mean ± SEM; n = 6 (C57BL/6 J) or 7 (NSG, Rag1^{-}) mice/ group. b. Weights of HY15549 tumors formed from cells constitutively expressing shRNAs against *LacZ* (control), *Sptlc1*, or *Sptlc2* and grown in C57BL/6 J mice. The tumors measured are shown below. On the right, immunoblot analysis of SPTLC1 (above) and SPTLC2 (below) in lysates from cells kept in culture or grown as tumors. Vinculin is used as a loading control. Mean ± SEM; n = 6 mice/ group. c. Weights of mixed population sgCTRL (gray) or sg*Sptlc1*-KO (pink) HY15549 tumors grown subcutaneously in C57BL/6 J or NSG mice. Mean ± SEM; n = 5 mice/ group. Images of tumors are shown below. Scale bar = 1 cm. Immunoblot analysis of SPTLC1 is shown above. GAPDH is used as a loading control. d. Weights of *Sptlc1*-KO (KO, pink) and *Sptlc1*-AB (AB, blue) HY15549 tumors orthotopically grown in the pancreas of C57BL/6 J mice. Mean ± SEM; n = 8 mice/ group. Image of tumors is shown below. Scale bar = 1 cm. X marks tumors that were not detected at the endpoint.

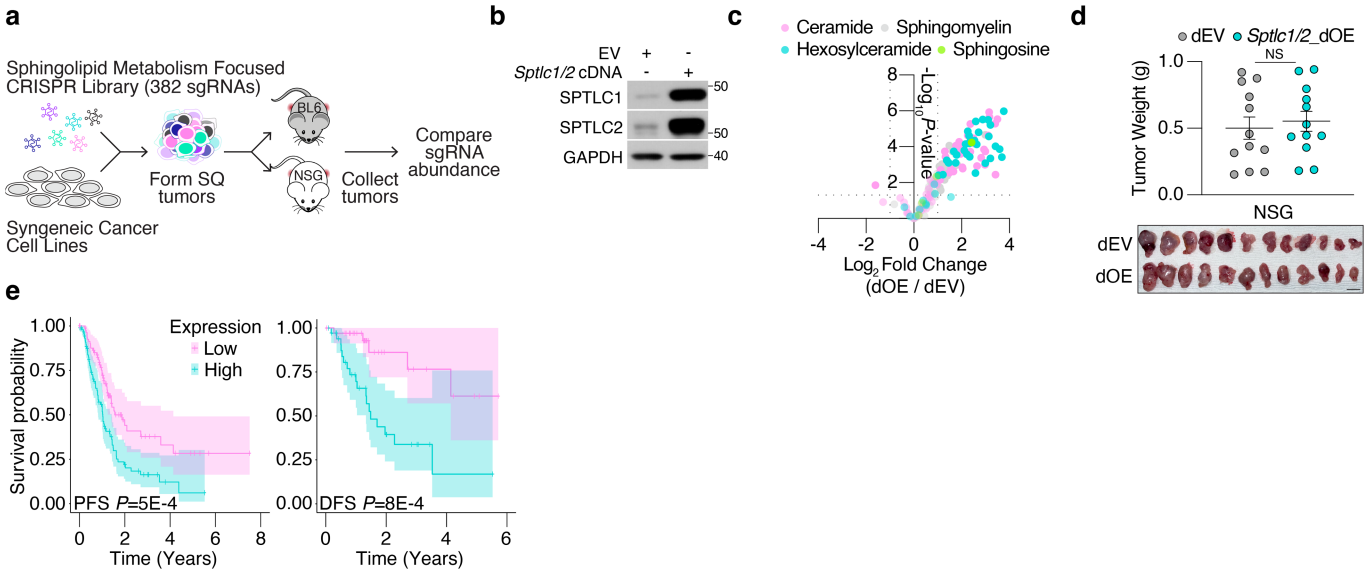

Extended Data Fig. 4 | Sphingolipid abundance mediates tumor control. a. Schematic of the sphingolipid metabolism focused CRISPR screen. Syngeneic cancer cell lines derived from C57BL/6 J mice were transduced with the sphingolipid metabolism library and injected subcutaneously (SQ) into the flanks of C57BL/6 J (B6) or NSG mice. Tumors were collected, their genomic DNA extracted, and guide RNA (sgRNA) abundance was determined. N ≥ 3 mice/ group. b. Immunoblot analysis of SPTLC1 and SPTLC2 in HY15549 cells overexpressing empty vectors or *Sptlc1* and *Sptlc2* cDNA. GAPDH is used as a loading control. c. Volcano plot showing $\log_2$ fold difference in ceramide-derived lipid species between double-empty vector wildtype (dEV) or *Sptlc1*/*Sptlc2* double-overexpression (dOE) HY15549 cells. d. Weights (top) and image (bottom) of double-empty vector wildtype (dEV) or *Sptlc1*/*Sptlc2* double-overexpression (*Sptlc1/2*_dOE) HY15549 tumors grown in NSG mice. Mean ± SEM, n = 6 mice/ group, scale bar = 1 cm. e. Progression (left) and disease (right) free survival analysis of TCGA PDAC patients with high (blue) or low (pink) expression of *SPTLC1*, *SPTLC2*, and *KDSR*. N = 177. Error bands = 95% confidence interval.

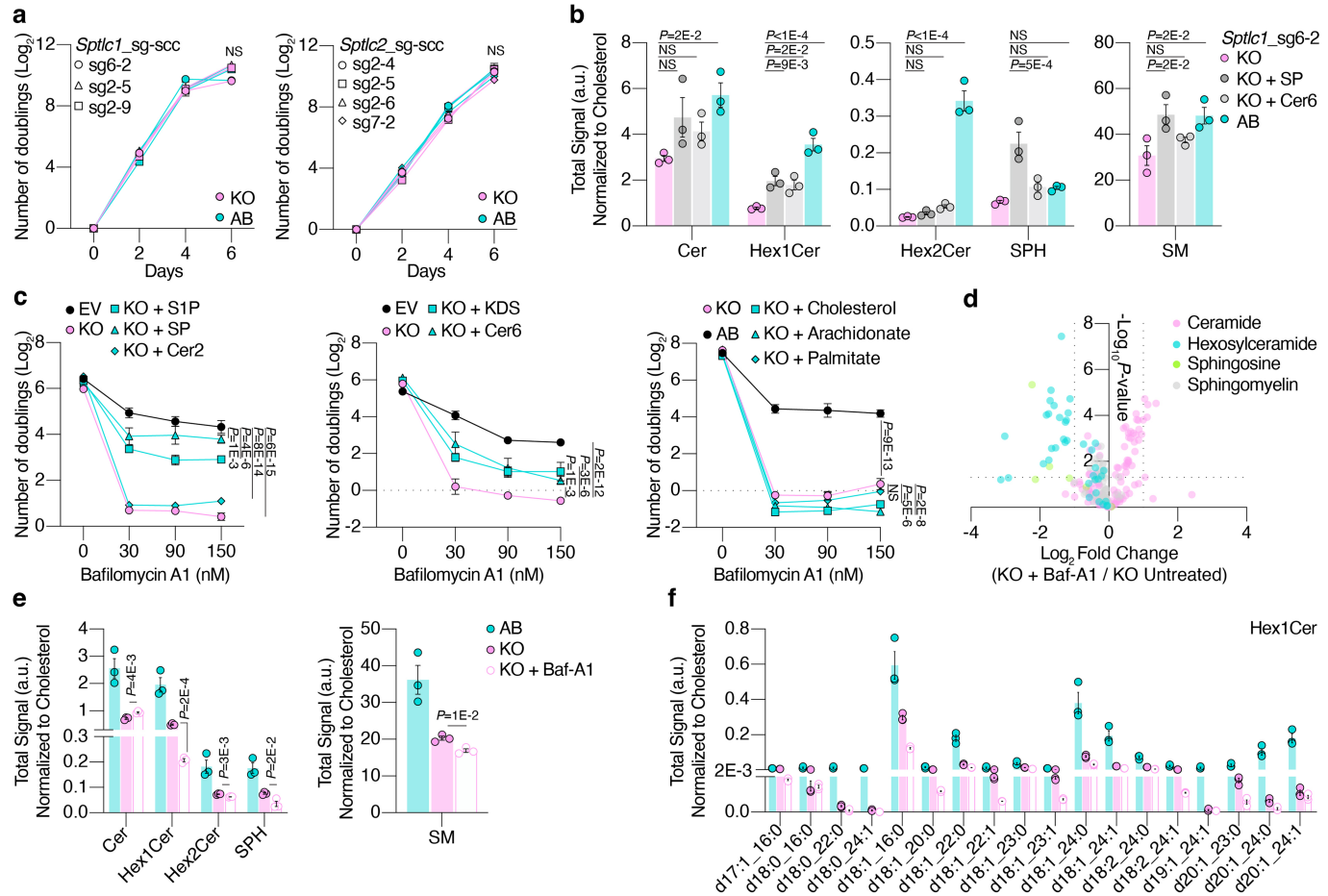

Extended Data Fig. 5 | Lysosomal sphingolipid salvage is sufficient to sustain cancer cell proliferation upon loss of de novo synthesis. a. Cell doublings over time of *Sptlc1* (left) or *Sptlc2* (right) KO (KO, pink) and AB (AB, blue) HY15549 cells grown in vitro. Different shapes are used to distinguish distinct KO/AB clonal pairs. Mean ± SD; n = 3 biological replicates. b. Abundance of ceramide-derived lipid species in *Sptlc1*_sg6-KO (KO) left untreated or supplemented with sphingosine or ceramide, and *Sptlc1*_sg6-AB (AB, blue) HY15549 cells. Abundance is normalized to cholesterol levels of each sample. Mean ± SEM, n = 3 biological replicates. c. Cell doublings of parental (EV, black), *Sptlc1*-KO (KO, pink), and KO HY15549 cells supplemented with sphingosine-1-phosphate (S1P, 1 µM, square), sphingosine (SP, 750 nM, triangle), C2-ceramide (Cer2, 5 µM, diamond), 3-ketodihydrosphingosine (KDS, 2 µM, square), C6-ceramide (Cer6, 1 µM, triangle), cholesterol (10 µM, square), arachidonate (10 µM, triangle), or palmitate (10 µM, diamond) and treated with increasing concentrations of Bafilomycin-A1. Mean ± SD; n = 3 biological replicates. d. Log_2 fold change of ceramide-derived lipid species abundance in *Sptlc1*_sg6-KO (KO) HY15548 cells left untreated or treated with bafilomycin-a1 (Baf-A1) relative to *Sptlc1*_sg6-AB (AB) cells. N = 3 biological replicates. e. Abundance of ceramide-derived lipid species in *Sptlc1*_sg6-KO (KO), left untreated or treated with Bafilomycin-A,1and *Sptlc1*_sg6-AB (AB, blue) HY15549 cells. Abundance is normalized to cholesterol levels of each sample. Mean ± SEM, n = 3 biological replicates. f. Abundance of hexosyl-1-ceramide species in *Sptlc1*_sg6-KO (KO), left untreated or treated with Bafilomycin-A,1and *Sptlc1*_sg6-AB (AB, blue) HY15549 cells. Abundance is normalized to cholesterol levels of each sample. Mean ± SEM, n = 3 biological replicates.

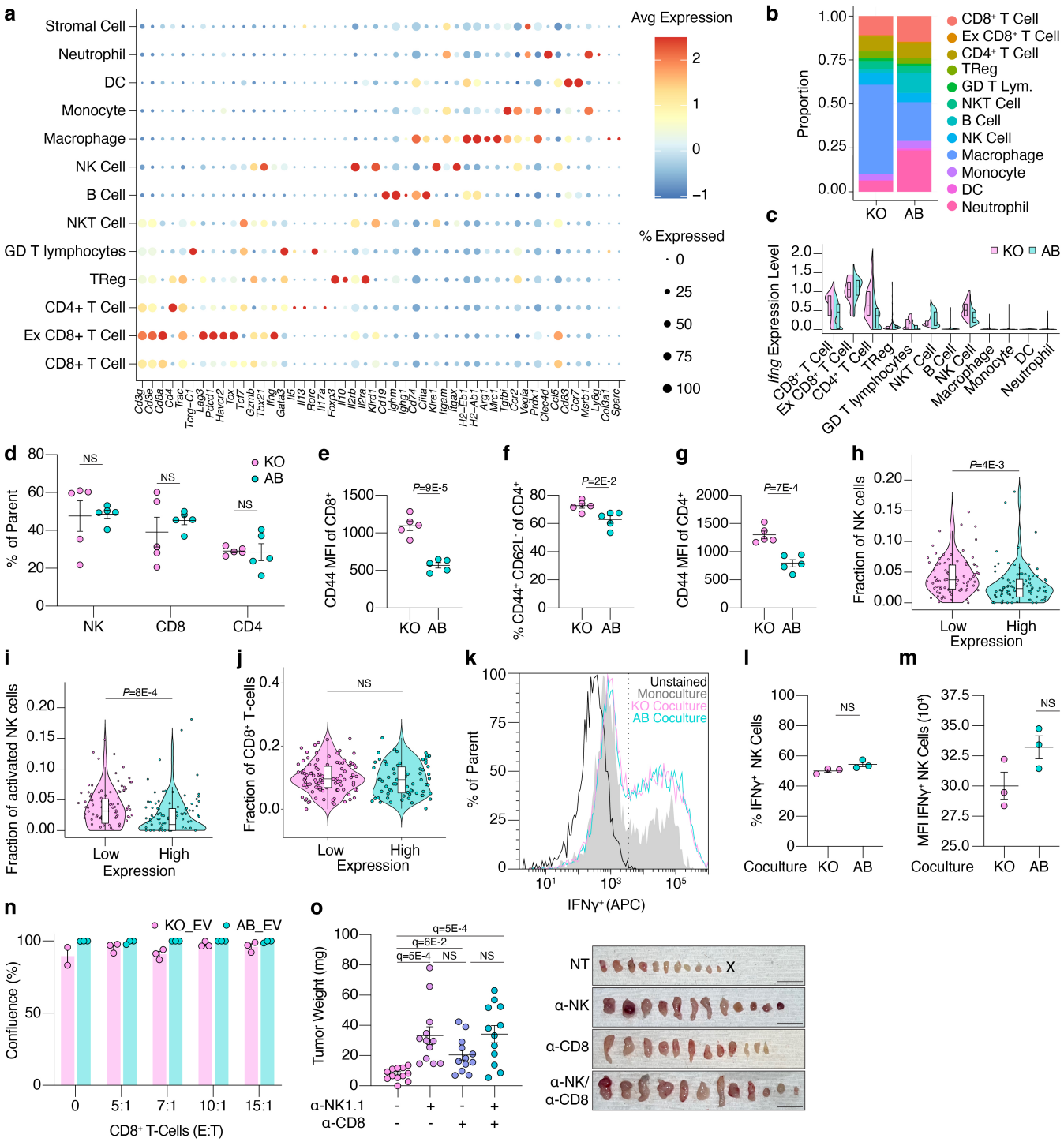

Extended Data Fig. 6 | See next page for caption.

Extended Data Fig. 6 | Sphingolipid depletion promotes inflammation in the tumor microenvironment. a. Differentially expressed genes used to annotate clusters (y-axis) of sequenced CD45$^+$ cells. Average expression is color-coded, and circle size corresponds to the percentage of cells within the cluster expressing the gene (x-axis). b. Bar plot showing relative differences in leukocyte infiltration in *Sptlc1*-KO (KO) and *Sptlc1*-AB (AB) tumors. c. Distribution of interferon-γ (*Ifng*) expression across distinct CD45$^+$ leukocyte populations isolated from *Sptlc1*-KO (pink) or *Sptlc1*-AB (blue) HY15549 tumors grown in C57BL/6 J mice. Data shown as mean ± SEM and analyzed by a two-sided Wilcoxon rank sum test with Benjamini-Hochberg correction. N = 5000 cells/ condition. Minima/maxima/center bounds are defined in the source data file. d. Flow analysis of relative proportions of NK, CD8$^+$ T, and CD4$^+$ T cells isolated from *Sptlc1*_sg6-KO (pink) or *Sptlc1*_sg6-AB (blue) HY15549 tumors grown in C57BL/6 J mice. Mean ± SEM; n = 5 mice/ group. e. Mean fluorescence intensity (MFI) of CD44 in CD8$^+$ T cells isolated from *Sptlc1*_sg6-KO (pink) or *Sptlc1*_sg6-AB (blue) HY15549 tumors grown in C57BL/6 J mice. Mean ± SEM; n = 5 mice/ group. f. Flow analysis of relative proportions of CD44$^+$/CD62L$^-$ CD4$^+$ T cells isolated from *Sptlc1*_sg6-KO (pink) or *Sptlc1*_sg6-AB (blue) HY15549 tumors grown in C57BL/6 J mice. Mean ± SEM; n = 5 mice/ group. g. MFI of CD44 in CD4$^+$ T cells isolated from *Sptlc1*_sg6-KO (pink) or *Sptlc1*_sg6-AB (blue) HY15549 tumors grown in C57BL/6 J mice. Mean ± SEM; n = 5 mice/ group. h. CIBERSORT analysis on TCGA expression data for PDAC tumors estimating the fraction of infiltrating NK cells in *SPTLC1*/*SPTLC2*/KDSR^{low} tumors (Low, pink) compared to *SPTLC1*/*SPTLC2*/*KDSR*^{high} (High, blue) tumors. N = 177 tumors. Minima/maxima/center bounds are defined in the source data file. i. CIBERSORT analysis on TCGA expression data for PDAC tumors estimating the fraction of activated infiltrating NK cells in *SPTLC1*/*SPTLC2*/KDSR^{low} tumors (Low, pink) compared to *SPTLC1*/*SPTLC2*/*KDSR*^{high} (High, blue) tumors. N = 177 tumors. Minima/maxima/center bounds are defined in the source data file. j. CIBERSORT analysis on TCGA expression data for PDAC tumors estimating the fraction of infiltrating CD8$^+$ T cells in *SPTLC1*/*SPTLC2*/*KDSR*^{low} tumors (Low, pink) compared to *SPTLC1*/*SPTLC2*/*KDSR*^{high} (High, blue) tumors. N = 177 tumors. Minima/maxima/center bounds are defined in the source data file. k. Histogram of IFNγ expression in NK cells monocultured or cocultured with *Sptlc1*_sg6-KO (pink) or *Sptlc1*_sg6-AB (blue) HY15549 cells. l. Percent of IFNγ$^+$ NK cells cocultured with *Sptlc1*_sg6-KO (pink) or *Sptlc1*_sg6-AB (blue) HY15549 cells. Mean ± SEM; n = 3 biological replicates. m. MFI of IFNγ$^+$ NK cells cocultured with *Sptlc1*_sg6-KO (pink) or *Sptlc1*_sg6-AB (blue) HY15549 cells. Mean ± SEM; n = 3 biological replicates. n. Proliferation of OVA-null *Sptlc1*_sg6-KO (KO_EV, pink) or *Sptlc1*_sg6-AB (AB_EV, blue) HY15549 cells left untreated or cocultured with OT-1 CD8$^+$ T cells at the indicated E:T ratios for 98 h. Mean ± SEM; n = 3 biological replicates. o. Weights and images of *Sptlc1*-KO HY15549 tumors grown in C57BL/6 J mice left untreated (NT), or treated with depleting antibodies for NK cells, CD8$^+$ T cells, or both. Mean ± SEM; n = 4 mice/ group. Scale bar = 1 cm. X marks tumors that were not detected at the endpoint. Analyzed using a one-way ANOVA with Benjamini-Hochberg multiple test correction.

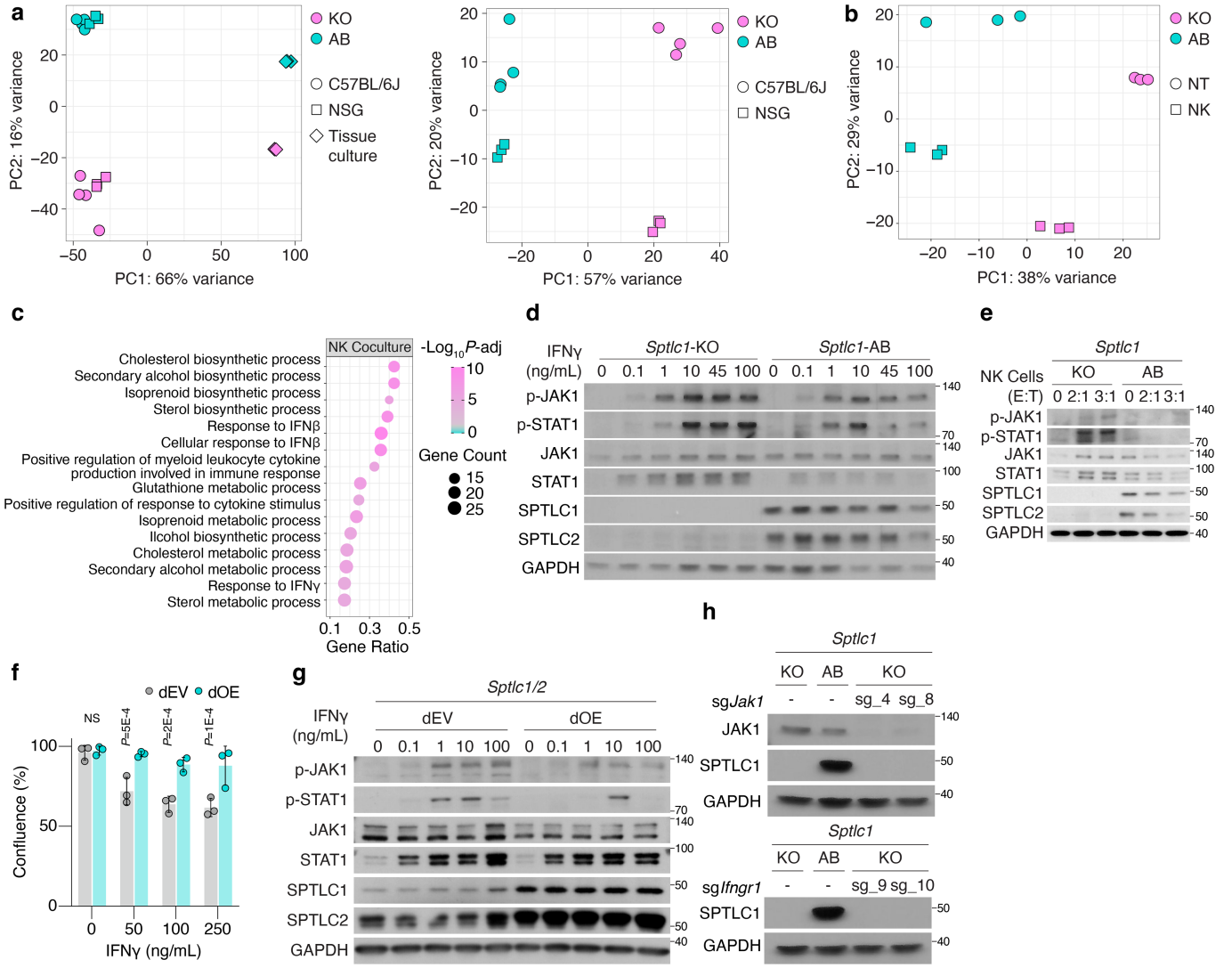

Extended Data Fig. 7 | Interferon signaling pathways are activated in *Sptlc1*-KO cells in the presence of immune pressure. a. PCA plot of RNA-seq from GFP$^+$ *Sptlc1*_sg6-KO (KO) and *Sptlc1*_sg6-AB (AB) HY15549 cells grown C57BL/6 J, NSG mice, or cultured in vitro (left) or in vivo (right). b. PCA plot of RNA-seq from *Sptlc1*_sg6-KO (KO) and *Sptlc1*_sg6-AB (AB) HY15549 cells left untreated or cocultured with NK cells (2:1 E:T ratio for 5 h). c. Gene set enrichment analysis of genes significantly higher in *Sptlc1*_sg6-KO versus *Sptlc1*_sg6-AB HY15549 cells left untreated or cocultured with NK cells (2:1 E:T ratio for 5 h). GO terms are ranked by gene ratio, adjusted *P*-values (FDR, -$\log_{10}$) are color-coded, and the circle size corresponds to the total number of genes in the gene set. d. Second example of an immunoblot analysis of interferon-γ signaling pathway induction in *Sptlc1*_sg6-KO and *Sptlc1*_sg6-AB HY15549 cells left untreated or treated with increasing concentrations of IFNγ for 4 h. GAPDH is a loading control. e. Second example of an immunoblot analysis of interferon-γ signaling pathway induction in *Sptlc1*_sg6-KO and *Sptlc1*_sg6-AB HY15549 cells cocultured with NK cells at the indicated E:T ratios for 5 h. GAPDH is a loading control. f. Proliferation of double-empty vector wildtype cells (dEV, gray) and *Sptlc1*/*Sptlc2* double-overexpression (dOE, blue) HY15549 cells treated with the indicated concentrations of IFNγ for 120 h. Mean ± SD; n = 3 biological replicates. g. Immunoblot of interferon-γ signaling pathway induction in double-empty vector wildtype cells (dEV) and *Sptlc1*/*Sptlc2* double-overexpression (dOE) HY15549 cells left untreated or treated with increasing concentrations of IFNγ for 4 h. GAPDH is a loading control. h. Immunoblot of of Jak1 in *Sptlc1*-KO (KO), *Sptlc1*-AB (AB) and *Sptlc1*_sg6/*Jak1*-KO (sg_4, sg_8) HY15549 cells (top) and Sptlc1 in *Sptlc1*_sg6-KO (KO), *Sptlc1*_sg6-AB (AB) and *Sptlc1*_sg6/*Ifngr1*-KO (sg_9, sg_10) HY15549 cells (bottom). GAPDH is a loading control.

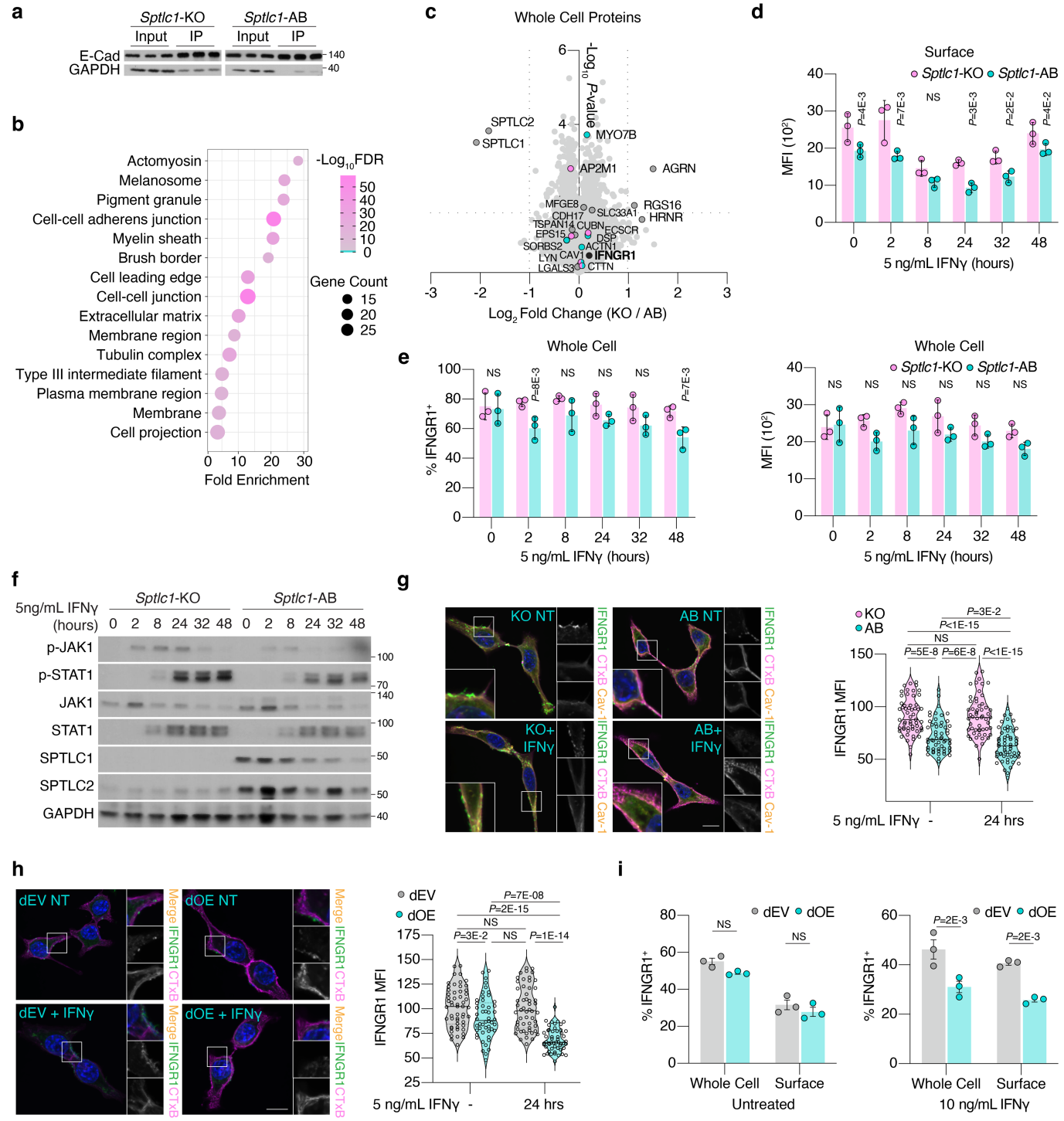

Extended Data Fig. 8 | See next page for caption.

Extended Data Fig. 8 | Sphingolipids impact plasma membrane expression of Ifngr1. a. Immunoblot of whole cell and biotinylated plasma membrane protein lysates from *Sptlc1*_sg6-KO and *Sptlc1*_sg6-AB HY15549 cells used for proteomic analysis. E-cadherin (E-cad) is a control for membrane enrichment and GAPDH is a marker for whole cell proteins. b. Gene set enrichment analysis of the top 206 (PSM > 20) most abundant proteins detected by LC-MS in biotinylated plasma membrane protein lysates. Jensen Compartments Ontology terms are ranked by fold enrichment, adjusted *P*-values (FDR, $-\log_{10}$) are color-coded, and circle size corresponds to the total number of genes in the gene set. c. Log_2 fold difference in whole cell proteins between *Sptlc1*_sg6-KO and *Sptlc1*_sg6-AB HY15549 cells versus $-\log_{10}$ *P*-value. d. Median fluorescence intensity of IFNGR1$^+$ *Sptlc1*_sg6-KO (pink) or *Sptlc1*_sg6-AB (blue) HY15549 cells treated with 5 ng/mL interferon-γ for the indicated times. Mean ± SD, n = 3 biological replicates. e. Flow analysis of IFNGR1 (left) and median fluorescence intensity (right) of IFNGR1 in permeabilized *Sptlc1*_sg6-KO (pink) and *Sptlc1*_sg6-AB (blue) HY15549 cells left untreated or treated with 5 ng/mL interferon-γ for the indicated times. Mean ± SD, n = 3 biological replicates. f. Immunoblot of interferon-γ signaling pathway induction in *Sptlc1*_sg6-KO and *Sptlc1*_sg6-AB HY15549 cells left untreated or treated with IFNγ for the indicated times. GAPDH is a loading control. g. Immunocytochemistry analysis of IFNGR1 and CAV1 in *Sptlc1*-KO (KO) and *Sptlc1*-AB (AB) HY15549 cells left untreated (top) or treated with 5 ng/mL IFNγ for 24 h. Choleratoxin B (CTxB) is used as a plasma membrane and sphingolipid abundance marker. Scale bar = 10 µm. Quantification of plasma membrane bound IFNGR1 is on the right, n = 55 cells/ condition. h. Immunocytochemistry analysis of IFNGR1 in double-empty vector wildtype cells (dEV) and *Sptlc1*/*Sptlc2* double-overexpression (dOE) HY15549 cells left untreated (top) or treated with 10 ng/mL IFNγ for 24 h. CTxB is used as a plasma membrane and sphingolipid abundance marker. Scale bar = 10 µm. Quantification of plasma membrane bound IFNGR1 is on the right, n = 50–54 cells/ condition. i. Flow analysis of whole cell and plasma membrane expression of IFNGR1 in double-empty vector cells (dEV, gray) and *Sptlc1*/*Sptlc2* double-overexpression (dOE, blue) HY15549 cells left untreated (left) or treated with 10 ng/mL IFNγ (right) for 24 h. Mean ± SEM; n = 3 biological replicates.

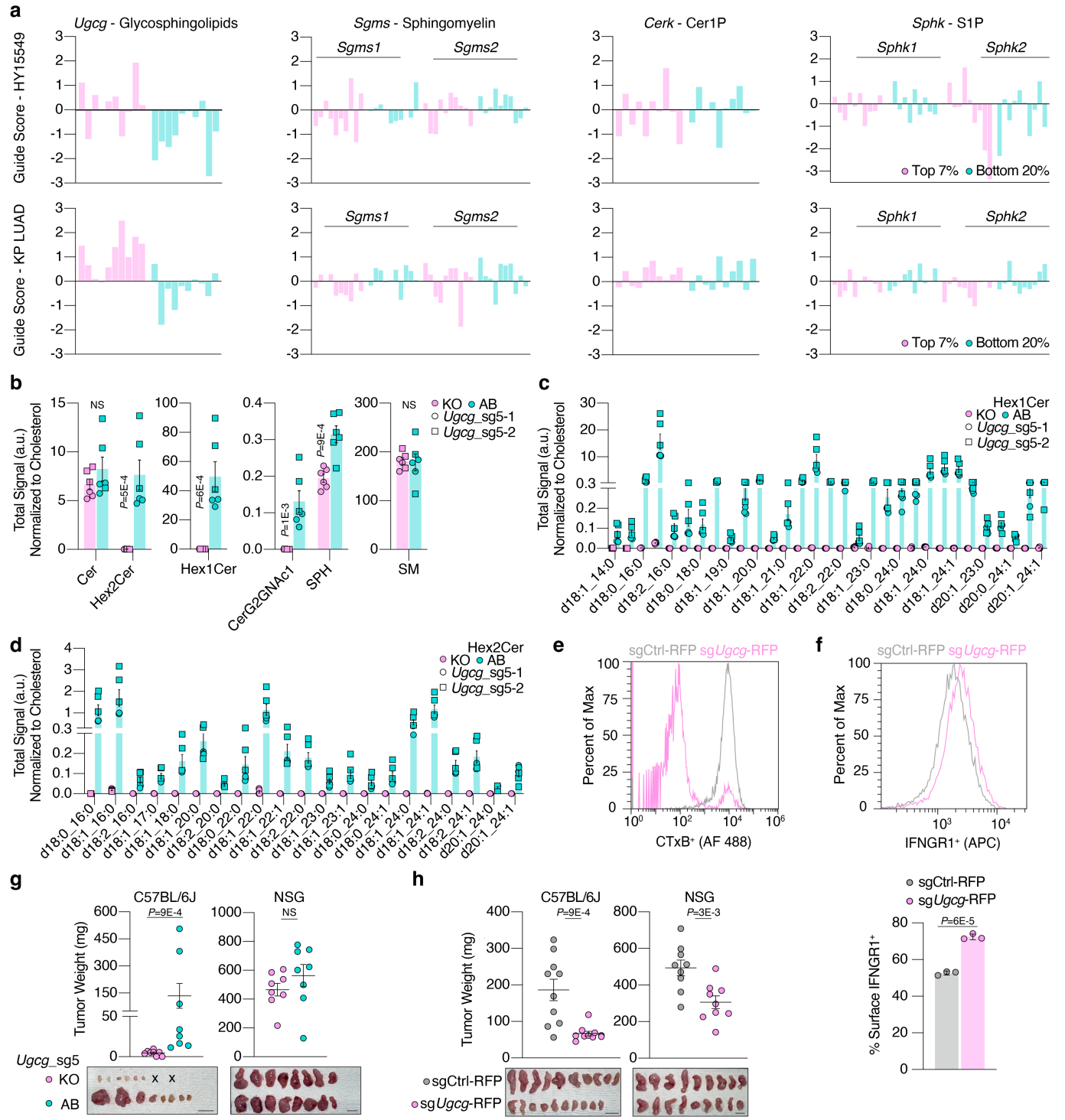

Extended Data Fig. 9 | De novo glycosphingolipid synthesis is limiting for cancer immune evasion. a. Guide scores of genes encoding enzymes at each branchpoint of sphingolipid synthesis. Guide scores of the top 7% (pink) and bottom 20% (blue) IFNGR1$^+$ HY15549 (top) and KP LUAD (bottom) cells transduced with the sphingolipid metabolism-focused sgRNA library are shown. b. Abundance of ceramide-derived lipid species in *Ugcg*_sg5-KO (KO) and *Ugcg*_sg5-AB (AB, blue) HY15549 cells. Signal is normalized to cholesterol levels of each sample. Mean ± SEM, n = 3 biological replicates. c. Abundance of hexosyl-1-ceramide species in *Ugcg*_sg5-KO (KO) and *Ugcg*_sg5-AB (AB, blue) HY15549 cells. Signal is normalized to cholesterol levels of each sample. Mean ± SEM, n = 3 biological replicates. d. Abundance of hexosyl-2-ceramide species in *Ugcg*_sg5-KO (KO) and *Ugcg*_sg5-AB (AB, blue) HY15549 cells. Signal is normalized to cholesterol levels of each sample. Mean ± SEM, n = 3 biological replicates. e. Flow analysis of plasma membrane glycosphingolipid levels measured by Choleratoxin B fluorescence (CTxB). f. Flow analysis of plasma membrane expression of IFNGR1 in sgCTRL-RFP and sg*Ugcg*-RFP HY15549 cells. Mean ± SEM; n = 3 biological replicates. g. Weights of *Ugcg*_sg5-KO (KO, pink) and *Ugcg*_sg5-AB (AB, blue) HY15549 tumors grown in NSG mice. Tumors measured are shown below. Mean ± SEM, n = 4 mice/group. h. Tumor weights of mixed population HY15549 cells expressing sgCTRL-RFP or sgUgcg-RFP grown in C57BL/6 J mice. Tumors measured are shown below. Mean ± SEM, n = 5 mice/group.

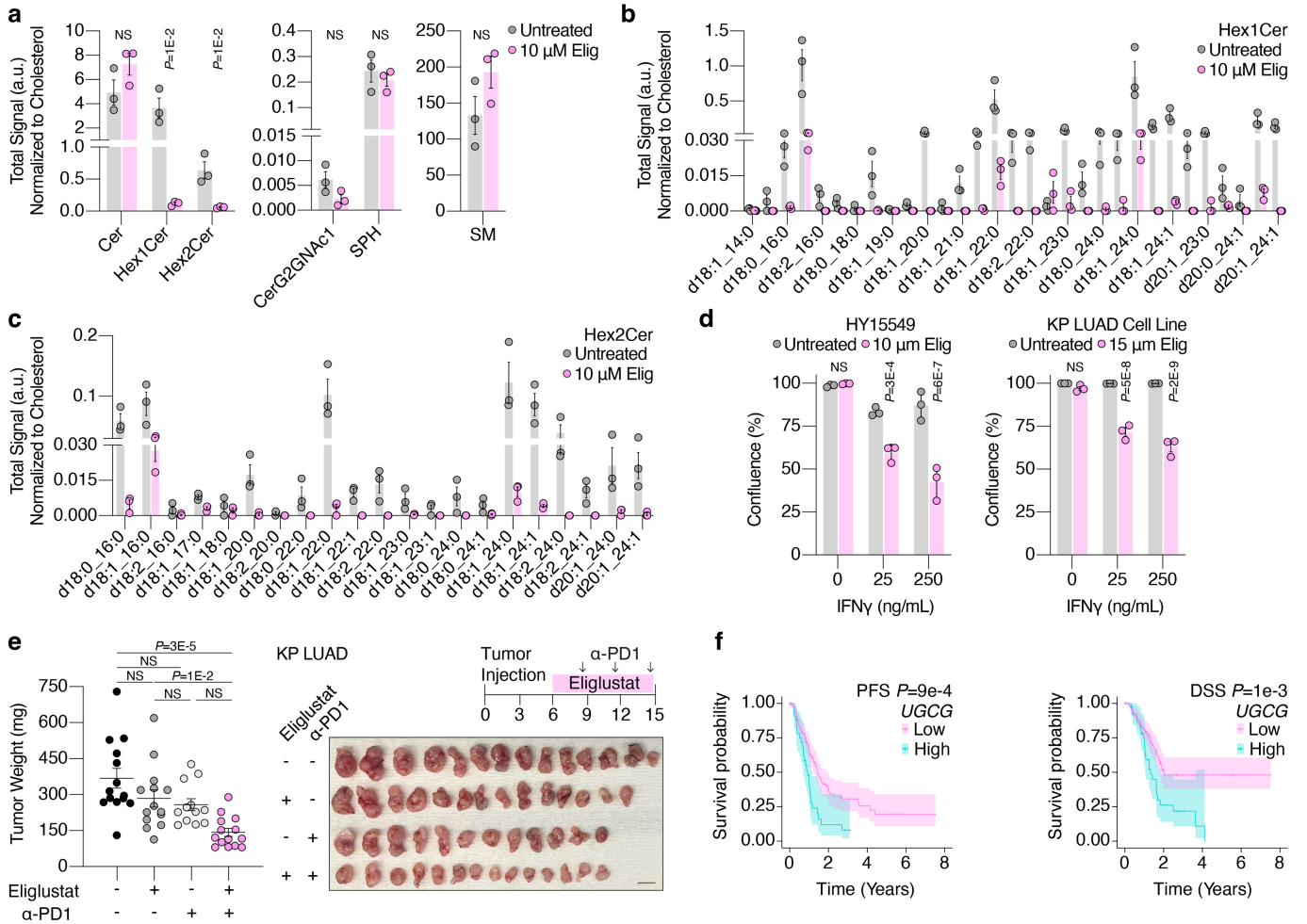

Extended Data Fig. 10 | Pharmacological depletion of glycosphingolipids impacts immune evasion. a. Abundance of ceramide-derived lipid species in HY15549 cells left untreated (gray) or treated with 10 µM eliglustat for 24 h. Signal is normalized to cholesterol levels of each sample. Mean ± SEM, n = 3 biological replicates. b. Abundance of hexosyl-1-ceramide species in HY15549 cells left untreated (gray) or treated with 10 µM eliglustat for 24 h. Signal is normalized to cholesterol levels of each sample. Mean ± SEM, n = 3 biological replicates. c. Abundance of hexosyl-2-ceramide species in HY15549 cells left untreated (gray) or treated with 10 µM eliglustat for 24 h. Signal is normalized to cholesterol levels of each sample. Mean ± SEM, n = 3 biological replicates. d. Proliferation of wildtype HY15549 (left) or KP LUAD (right) cells left untreated (gray) or pretreated with eliglustat for 24 h (pink) and the indicated concentrations of interferon-γ (IFNγ) for 96 h. Mean ± SD; n = 3 biological replicates. e. Weights (left) and image (right) of wildtype KP LUAD tumors grown in C57BL/6 J mice on the indicated treatment regimens. Mean ± SEM; n = 6 (HY15549 −/−, +/−, −/+, KPLUAD −/+) or 7 (others) mice/ group; scale bar = 1 cm. Data were analyzed using a one-way ANOVA with Tukey's multiple test correction. f. Survival analysis of TCGA PDAC patients with high (blue) or low (pink) expression of *SPTLC1*, *SPTLC2*, and *KDSR*. N = 177. Error bands = 95% confidence interval.

nature portfolio

Corresponding author(s): Kivanc Birsoy

Last updated by author(s): Jun 24, 2024

Reporting Summary

Nature Portfolio wishes to improve the reproducibility of the work that we publish. This form provides structure for consistency and transparency in reporting. For further information on Nature Portfolio policies, see our Editorial Policies and the Editorial Policy Checklist.

Statistics

For all statistical analyses, confirm that the following items are present in the figure legend, table legend, main text, or Methods section.

n/a	Confirmed	
☐	☒	The exact sample size (*n*) for each experimental group/condition, given as a discrete number and unit of measurement
☐	☒	A statement on whether measurements were taken from distinct samples or whether the same sample was measured repeatedly
☐	☒	The statistical test(s) used AND whether they are one- or two-sided *Only common tests should be described solely by name; describe more complex techniques in the Methods section.*
☒	☐	A description of all covariates tested
☐	☒	A description of any assumptions or corrections, such as tests of normality and adjustment for multiple comparisons
☐	☒	A full description of the statistical parameters including central tendency (e.g. means) or other basic estimates (e.g. regression coefficient) AND variation (e.g. standard deviation) or associated estimates of uncertainty (e.g. confidence intervals)
☐	☒	For null hypothesis testing, the test statistic (e.g. *F*, *t*, *r*) with confidence intervals, effect sizes, degrees of freedom and *P* value noted *Give P values as exact values whenever suitable.*
☒	☐	For Bayesian analysis, information on the choice of priors and Markov chain Monte Carlo settings
☒	☐	For hierarchical and complex designs, identification of the appropriate level for tests and full reporting of outcomes
☒	☐	Estimates of effect sizes (e.g. Cohen's *d*, Pearson's *r*), indicating how they were calculated

Our web collection on statistics for biologists contains articles on many of the points above.

Software and code

Policy information about availability of computer code

Data collection	For lipidomics Q Exactive (Thermo Scientific). For flow cytometry data: Attune NxT and BD FACSymphony. For proteomics: Easy nLC 1200 HPLC. Confocal images were acquired using Nikon A1R MP multiphoton microscope or Zeiss LSM 710 laser scanning confocal microscope.
Data analysis	Screens were analyzed using Python (v.2.7.13), R (v.3.3.2), and Unix (v.4.10.0-37-generic x86_64). For lipidomics, LipidSearch software was used. For Proteomics, Sequest HT, Perseus and Proteome Discoverer v. 2.5 were used. For RNA sequencing, CIBERSORT, and survival analyses, R was used. Flow cytometry experiments were analyzed using Attune NxT software, FlowJo, and FCS Express 7. All other statistical analyses were perfomed on GraphPad Prism 7, 8, or 10. Confocal images were analyzed with FIJI (ImageJ2, Version 2.3.0).

For manuscripts utilizing custom algorithms or software that are central to the research but not yet described in published literature, software must be made available to editors and reviewers. We strongly encourage code deposition in a community repository (e.g. GitHub). See the Nature Portfolio guidelines for submitting code & software for further information.

Data

Policy information about availability of data

All manuscripts must include a data availability statement. This statement should provide the following information, where applicable:

- Accession codes, unique identifiers, or web links for publicly available datasets
- A description of any restrictions on data availability
- For clinical datasets or third party data, please ensure that the statement adheres to our policy

Proteomics data have been deposited to the ProteomeXchange Consortium with the dataset identifier PXD052718. scRNA-seq data has been deposited to NCBI's Gene Expression Omnibus and can be accessed with the accession number GSE270660. Source data have been included with this paper. For RNAseq analysis, the publicly available mouse reference genome mm10 UCSC (v1.4.0) was used. For gene set enrichment analysis, the publicly available site, AmiGO 2, was used. Patient data from PDAC tumors were obtained from the The Cancer Genome Atlas (TCGA) Pan-cancer dataset via the cBio Cancer Genomics Portal.

Human research participants

Policy information about studies involving human research participants and Sex and Gender in Research.

Reporting on sex and gender	NA
Population characteristics	NA
Recruitment	NA
Ethics oversight	NA

Note that full information on the approval of the study protocol must also be provided in the manuscript.

Field-specific reporting

Please select the one below that is the best fit for your research. If you are not sure, read the appropriate sections before making your selection.

☒ Life sciences ☐ Behavioural & social sciences ☐ Ecological, evolutionary & environmental sciences

For a reference copy of the document with all sections, see nature.com/documents/nr-reporting-summary-flat.pdf

Life sciences study design

All studies must disclose on these points even when the disclosure is negative.

Sample size	For in vitro assays, n = 3 biological replicates were used for reliability and to enable statistical analyses. Sample sizes for in vivo assays were determined from understanding variability within the first pilot studies. Based on these results, it was determined that at least 6 tumors in each group would be sufficient to determine statistical significance, or lack thereof, with greater than 80% power and holding Type I Error to 5%. All experiments were repeated at least twice with similar results observed.
Data exclusions	For CRISPR/Cas9 genetic screens, gene scores derived from 3 or less guide scores were excluded from the analysis. For the rest of the experiments, no data was excluded.
Replication	All in vitro experiments were repeated at least 3 times and in vivo experiments were repeated at least twice with similar outcomes. Both technical and biological replicates were reliably reproduced.
Randomization	Sample groups were allocated randomly.
Blinding	For in vivo experiments but not in vitro experiments, the investigators were blinded during data collection and analysis.

Reporting for specific materials, systems and methods

We require information from authors about some types of materials, experimental systems and methods used in many studies. Here, indicate whether each material, system or method listed is relevant to your study. If you are not sure if a list item applies to your research, read the appropriate section before selecting a response.

Materials & experimental systems

n/a	Involved in the study
☐	☒ Antibodies
☐	☒ Eukaryotic cell lines
☒	☐ Palaeontology and archaeology
☐	☒ Animals and other organisms
☒	☐ Clinical data
☒	☐ Dual use research of concern

Methods

n/a	Involved in the study
☒	☐ ChIP-seq
☐	☒ Flow cytometry
☒	☐ MRI-based neuroimaging

Antibodies

Antibodies used

Gapdh (GeneTex #GTX627408), Sptlc1 (Proteintech #15376-1-AP) Sptlc2 (Proteintech 51012-2-AP), IFNGR1 (Proteintech #10808-1-AP), p-Stat1 (R&D Systems #AF2894-SP), Stat1 (Cell Signaling Technology #14994T), Jak1 (Cell Signaling Technology #3344S), p-Jak1 (Cell Signaling Technology #3331S), e-Cadherin (Cell Signaling Technology #14472S), B-actin (GeneTex #GTX109639) and Cav-1 (Cell Signaling Technologies #3238S) anti-mouse IgG-HRP (Cell Signaling Technology #7076), anti-rabbit IgG-HRP (Cell Signaling Technology #7074), APC-CD119 (Miltenyi Biotec #130-104-935), CD16/32 (2.4G2, BioXcell) IFNGR1 (1:200, Invitrogen #PA5-27841) anti-caveolin CoraLite588 conjugate (Proteintech #CL488-66067), Alexa Fluor 488 conjugated anti-rabbit (ThermoFisher, A32790), pan-keratin (Cell Signaling Technology, #4545T), anti-NK1.1 (Bio X Cell #BE0036), anti-CD8 (Bio X Cell #BE0004-1)

Validation

All antibodies used in this study are commercially available and have been validated by the manufacturer, other groups in published works, or our own laboratory. For SPTLC1 and SPTLC2, antibodies were validated using wild type, clonal knockout, and cDNA expressing cell lines.

Eukaryotic cell lines

Policy information about cell lines and Sex and Gender in Research

Cell line source(s)

HEK293T cells were obtained from ATCC. HY15549 cells were obtained from Dr. Nabeel M. Bardeesy (Massachusetts General Hospital Cancer Center), KP LUAD cells were obtained from Dr. Thales Papagiannakopoulos (New York University), and MC38 cells were obtained from Kerafast (Boston, MA).

Authentication

HEK293T cells were authenticated via STR profiling. HY15549 and KP LUAD cell lines were not authenticated as they were generated at and obtained from their lab of origin.

Mycoplasma contamination

PCR analysis confirming the absence of mycoplasma contamination was performed routinely every 6 months.

Commonly misidentified lines
(See ICLAC register)

No commonly misidentified cell lines were used.

Animals and other research organisms

Policy information about studies involving animals; ARRIVE guidelines recommended for reporting animal research, and Sex and Gender in Research

Laboratory animals

C57BL/6J (#000664), NSG (#005557), B6.129S7-Rag1tm1Mom/J (#002216), B6.129S7-Ifngtm1Ts/J (#002287), C57BL/6-Tg(TcraTcrb)1100Mjb/J (#003831) were obtained from The Jackson Laboratory. All mice were 6-10 weeks of age. All mice were maintained on a standard light-dark cycle with food and water ad libitum. The room was maintained at a controlled temperature (23-24°C) and humidity (60.5%). Cages were cleaned every 4-5 days and supplies of water and food were checked daily.

Wild animals

The study did not involve the use of wild animals.

Reporting on sex

All syngeneic cell lines were grown in mice of the same sex as the cell line of origin to avoid confounding inflammatory responses.

Field-collected samples

The study did not involve the use of field-collected samples.

Ethics oversight

All mouse experiments were conducted in accordance with a protocol approved by the Institutional Animal Care and Use Committee at The Rockefeller University.

Note that full information on the approval of the study protocol must also be provided in the manuscript.

Flow Cytometry

Plots

Confirm that:

☒ The axis labels state the marker and fluorochrome used (e.g. CD4-FITC).

☒ The axis scales are clearly visible. Include numbers along axes only for bottom left plot of group (a 'group' is an analysis of identical markers).

☒ All plots are contour plots with outliers or pseudocolor plots.

☒ A numerical value for number of cells or percentage (with statistics) is provided.

Methodology

Sample preparation	Flow Cytometry Analysis of Ifngr1 500,000 cells were collected and washed once with PBS. For extracellular staining, cells were resuspended in 50 µL FACS buffer containing 1:10 antibody (Miltenyi Biotec #130-104-935) and incubated in the dark at 4°C for 15 minutes. To wash cells, 1 mL of FACS buffer (PBS, 1% BSA, 5mM EDTA) was added to each sample before centrifugation at 500 X g for 5 minutes at 4°C. Pellets were resuspended in FACS buffer with DAPI and immediately analyzed on an Attune NxT (Thermo Scientific). For intracellular staining, 500,000 cells were collected and washed once with PBS. To fix and permeabilize the cells, samples were resuspended in 50 µL of PBS and 200 µL of 100% ice cold methanol was added dropwise while gently vortexing. Cells were incubated in 80% methanol on ice for 20 minutes. Then, 1 mL of PBS was added, and cells centrifuged at 500 X g for 5 minutes at 4°C. Ifngr1 staining and acquiring proceeded as above. Flow Cytometry Analysis of Tumor Infiltrating Immune Cells Tumors were excised and digested for 1 hour at 37°C with with 400U/mL of collagenase D (Roche) and 0.2 µg/mL DNase I (Sigma). Digested tumors were filtered through 70 µm filters. Enrichment of hematopoietic cells was achieved by density gradient centrifugation with 40%/90% Percoll (GE Healthcare Life Sciences) for 25 minutes at 2500 RPM at 22°C without breaks. The interphase containing hematopoietic cells was isolated and washed with PBE. Red blood cell lysis was performed with ACK lysis buffer (GIBCO). For cytokine staining, cells were incubated at 37°C for 4 hours in complete RPMI media supplemented with Brefeldin A (Sigma), phorbol 12-myristate 13-acetate (PMA) (Sigma) and Ionomycin (Sigma). Following incubation, cells were washed with PBE. Cells were incubated for 5 minutes with 1 µg/mL of anti-CD16/32 (2.4G2, BioXcell) at room temperature. Cells were washed with PBS and stained with Zombie fixable viability dye (Biolegend) for 15 minutes at room temperature. Cells were washed with PBE and stained with appropriate surface marker antibodies for CD4+ and CD8+ T cells and NK cells for 20 minutes at 4°C. Cells were washed with PBE, fixed, and permeabilized (Cytofix/Cytoperm kit, BD). Intracellular staining for IFNγ was performed for 30 minutes at 4°C. Cells were washed and resuspended in PBE. Samples were acquired on a BD FACSymphony and data were analyzed using FlowJo v.10.6.2 software. Flow Cytometry Analysis of IFNγ in NK Cells 20,000 GFP-expressing target cells were plated in each well of a round bottom 96-well plate. NK cells were isolated as above and added to target cells at a 3:1 ratio in the presence of IL-15, IL-2, and IL-12. After an overnight incubation, each well was treated with Brefeldin-A (BioLegend 420601) for 4 hours. After, NK cells were collected, washed, and permeabilized using the BD Cytofix/Cytoperm kit (BD BioSciences 554714) following the manufacturer's instructions. NK cells were stained on ice for 20 minutes with primary antibody (1:200, Thermo Scientific 17-7311-81). Samples were acquired using Attune NxT (Thermo Scientific).
Instrument	Attune NxT (Thermo Scientific) and BD FACSymphony
Software	Attune NxT, FlowJo, and FCS Express
Cell population abundance	For the Ifngr1 CRISPR screen, the top 7% and bottom 20% fluorescent cells were collected. For cell sorting involving the collection of transduced cells to generate knockout or control cell lines, the top 10% fluorescent populations were collected. A minimum of 50,000 cells were collected in each case.
Gating strategy	For all experiments, dead cells were excluded using DAPI or Zombie fixable viability dye (Biolegend). Live cells were further gated to include only singlets, determined by forward and side scatter plots.

☒ Tick this box to confirm that a figure exemplifying the gating strategy is provided in the Supplementary Information.